

# **Ionospheric Total Electron Content Variability and its influence in Radio Astronomy**

A thesis submitted in partial fulfillment of the requirements for the degree of

**Master of Science**

of

**Rhodes University**

(South Africa)

by

Botai Ondego Joel

October, 2005

### **Declaration**

I declare that to the best of my knowledge, this thesis is my own work and that it has not been submitted in any form for another degree or diploma at any university or other institution of tertiary education. Information derived from published or unpublished work of others has been acknowledged in the text and a list of references is given.

## **Acknowledgements**

There are a number of people who helped me complete this project. I would like to thank the following; My supervisor Prof. A. Poole., and co-supervisor Dr. Pierre Cilliers as well Dr. Lee-Anne McKinnell; Dr. Peter Sutcliffe and entire staff of the HMO; Prof. Peter Dunsby and his entire staff and my fellow NASSP students. I also express my gratitude to the Department of Physics and Electronics and generally Rhodes University for their support during my dissertation period. To the NRF and Ford Foundation, thanks for awarding me a bursary. I would like to acknowledge HartRAO Space Geodesy Programme group for their support during the final touches of this thesis. Little one Michael, thanks for being with me. Those who helped me in one way or another and I have not mentioned you, please you are in the list. I am grateful to you all.

## Abstract

Ionospheric phase delays of radio signals from Global Positioning System (GPS) satellites have been used to compute ionospheric Total Electron Content ( $TEC$ ). An extended Chapman profile model is used to estimate the electron density profiles and  $TEC$ . The Chapman profile that can be used to predict  $TEC$  over the mid-latitudes only applies during day time. To model night time  $TEC$  variability, a polynomial function is fitted to the night time peak electron density profiles derived from the online International Reference Ionosphere (IRI) 2001. The observed and predicted  $TEC$  and its variability have been used to study ionospheric influence on Radio Astronomy in South Africa region. Differential phase delays of the radio signals from Radio Astronomy sources have been simulated using  $TEC$ . Using the simulated phase delays, the azimuth and declination offsets of the radio sources have been estimated. Results indicate that, pointing errors of the order of miliarcseconds ( $mas$ ) are likely if the ionospheric phase delays are not corrected for. These delays are not uniform and vary over a broad spectrum of timescales. This implies that fast frequency (referencing) switching, closure phases and fringe fitting schemes for ionospheric correction in astrometry are not the best option as they do not capture the real state of the ionosphere especially if the switching time is greater than the ionospheric  $TEC$  variability. However, advantage can be taken of the GPS satellite data available at intervals of a second from the GPS receiver network in South Africa to derive parameters which could be used to correct for the ionospheric delays. Furthermore GPS data can also be used to monitor the occurrence of scintillations, (which might corrupt radio signals) especially

for the proposed, Square Kilometer Array (SKA) stations closer to the equatorial belt during magnetic storms and sub-storms. A 10 minute snapshot of GPS data recorded with the Hermanus [34.42<sup>0</sup> S, 19.22<sup>0</sup> E] dual frequency receiver on 2003-04-11 did not show the occurrence of scintillations. This time scale is however too short and cannot be representative. Longer time scales; hours, days, seasons are needed to monitor the occurrence of scintillations.

# Contents

<b>1</b>	<b>Introduction</b>	<b>1</b>
<b>2</b>	<b>Ionospheric Interactions with extra-terrestrial radio waves</b>	<b>5</b>
2.1	Introduction . . . . .	5
2.2	Radio signal interactions with ionosphere . . . . .	6
2.3	Characterising the ionosphere . . . . .	10
<b>3</b>	<b>Total Electron Content (<i>TEC</i>) Variability</b>	<b>19</b>
3.1	Introduction . . . . .	19
3.2	<i>TEC</i> Variability . . . . .	19
3.3	Methods of estimating <i>TEC</i> variability . . . . .	21
<b>4</b>	<b>Ionospheric Correction Techniques, suitable for the SKA</b>	<b>31</b>
4.1	Introduction . . . . .	31
4.2	An Interferometer receiver system . . . . .	32
4.3	The Phase Equation . . . . .	43
4.4	Simulation of the effects of <i>TEC</i> variability on pointing accuracy of a radio source . . . . .	45
4.5	Ionospheric Scintillations . . . . .	50
<b>5</b>	<b>Results and Discussion</b>	<b>52</b>
5.1	Introduction . . . . .	52
5.2	Predicted sTEC at different locations within the pro- posed SKA region using the extended Chapman profile	52
5.3	GPS derived <i>TEC</i> . . . . .	66

5.4	Pointing errors due to phase delay . . . . .	73
<b>6</b>	<b>Conclusion</b>	<b>75</b>
<b>7</b>	<b>Appendix : Transformations</b>	<b>78</b>
7.1	ECEF, Geocentric and Geodetic coordinate systems .	78
7.2	Satellite Orbit-coordinate systems. . . . .	85
7.2.1	Satellite Orbit-plane . . . . .	86
7.2.2	Right Ascension-Declination coordinate system	88
7.2.3	Satellite Orbit orientation in space . . . . .	89
7.2.4	Azimuth-Elevation coordinate system . . . . .	92
7.3	Satellite coordinate system transformation . . . . .	93

## List of Tables

1	Scientific specifications of Square Kilometer Array, [Taylor, 1999]. . . . .	2
2	Ionospheric perturbations for a column density of $10^{17} \frac{\text{electrons}}{m^2}$	5
3	Predicted peak differential sTEC dependence on baseline length between radio telescopes with an East-West configuration on 2003-04-11 along azimuth $35^0$ over latitude [ $25^0$ S]. . . . .	62
4	<i>TEC</i> (in TECU) values on 2003-04-11 at 00H00. . . . .	67
5	<i>TEC</i> (in TECU) values on 2003-04-11 at 06H00. . . . .	67
6	<i>TEC</i> (in TECU) values on 2003-04-11 at 12H00. P1 value for satellite SV.6 was not present. . . . .	68
7	<i>TEC</i> (in TECU) values on 2003-04-11 at 18H00. . . . .	68
8	Predicted radio source pointing errors induced by the ionosphere computed by the extended Chapman profile. The pointing errors are in order of milliarcseconds <i>mas</i> as reported in literature [P�ere-Torres et al, 2000]. . . . .	73
9	GPS derived sTEC effect on radio source pointing errors. The pointing errors are higher in order of magnitude to those predicted by the extended Chapman model. . . . .	74
10	WGS84 Ellipsoid Parameters . . . . .	80
11	Geocentric conversion to ECEF coordinates . . . . .	81
12	ECEF conversion to Geocentric coordinates . . . . .	81
13	Conversion from Geocentric to Geodetic and back to Geocentric coordinates. . . . .	86

## List of Figures

1	Magnetic field $\mathbf{B}$ inclined $\theta^0$ with the z-axis. The Transverse of Lorentz force is ignored at much higher frequencies. . . . .	8
2	The $\alpha$ -Chapman profile for the vertical electron density variation. The loss mechanism is through direct attachment to positive ion species. The different curves depict the effect of solar zenith angle, in degrees, on total electron densities in the ionosphere. . . . .	13
3	The $\beta$ -Chapman profile for the vertical electron density variation. The equilibrium condition is affected by loss of electrons through attachment to neutral molecules. The different curves show the variation of electron density in the ionosphere with solar zenith angle in degrees. . . . .	14
4	Mid-latitude ionosphere structure during the summer day. Main ionizing radiations are indicated. Taken from Davies [1990]. .	17
5	Night time IRI 2001, Model function, and GPS based vTEC at Simonstown, [33.19 <sup>0</sup> S, 18.44 <sup>0</sup> E] location on 2003-03-13. . .	22
6	Variation of sun Zenith angle from [25 <sup>0</sup> S, 20 <sup>0</sup> E] on 2003-04-11.	23
7	Diurnal $TEC$ derived from the Chapman profile from [34.24 <sup>0</sup> S, 19.26 <sup>0</sup> E] on 2005-05-05. The solar zenith angles are fixed to 70 <sup>0</sup> , 75 <sup>0</sup> , 80 <sup>0</sup> , and 85 <sup>0</sup> . . . . .	24

8	vTEC derived from IRI 2001 data compared with <i>TEC</i> reconstructed from Fourier series. Figure 8(a) shows the diurnal variation on 2001-03-14 while Figure 8 (b) shows variations on 2005-03-14. These results were calculated from a location with geographical coordinates, [34.22° S, 19.24° E]. . . . .	25
9	Electron density profiles derived using the on-line IRI 2001 model on 2003-04-11 for a location at [30.0° S, 20.0° E] along 20° and 35° elevation and azimuth angles respectively. Figure by Cilliers, [2005]. . . . .	26
10	Electron density profiles derived using the extended Chapman profile on 2003-04-11 for a location at [30.0° S, 20.0° E] along 20° and 35° elevation and azimuth angles respectively. . . . .	27
11	Derived peak electron density versus solar zenith angles as predicted from [25° S, 20° E] along 20°, and 35° elevation and azimuth angles respectively on 2003-04-11. $1\text{NU}=10^{12} \frac{\text{electrons}}{\text{m}^3}$ . These are two curves but are superimposed to give the variation over a complete day. . . . .	29
12	Night time vTEC computed from IRI 2001, the Fourier function as well as extended Chapman function. The Fourier function and the extended Chapman function use coefficients derived from the IRI 2001 data. . . . .	30
13	Conversion of RF to IF and phase lock stage. The phase lock system sends an error signal to the LO for correction . . . . .	33

14	Block diagram for the correlation stage of a radio signal allows the measurement of both the cosine and sine components simultaneously. . . . .	36
15	Fringe Visibility dependence on the baseline vector. A double point source is convolved with a single point source to form a double extended source. The visibility reduces with an increase in the baseline vector. The fringe spacing, in radians, ( angular distance between successive maxima ) is given by $nB_\lambda = \sin \theta_{ab}$ , where $n = 0, \pm 1, \pm 2, \pm 3, \dots$ . If $\theta_{ab}$ is small, the fringe spacing is given by $\Delta\theta_{ab} \approx \frac{1}{B_\lambda}$ . But if $\theta_{ab}$ is large, the expression for fringe spacing would be $\Delta\theta_{ab} \approx \frac{1}{B_\lambda \cdot \cos \theta_{ab}}$ . . . . .	37
16	East-West orientation, and the fringes on the u-v plane, (a spatial plane in the sky perpendicular to the vector $\vec{s}$ ). The fringe pattern is parallel to the right ascension of the source, (on the u-axis). . . . .	38
17	North-South orientation of an interferometer baseline, and the fringes on the u-v plane. The fringes are on the v-axis, (parallel to the direction of the declination of the radio source). . . . .	39
18	The fringe pattern for which the interferometer baseline orientation is at an arbitrary angle from the North-South geometry. . . . .	40
19	Possible SKA sites in Southern Africa. Most of these stations are positioned alongside GPS receivers. . . . .	53
20	Predicted diurnal sTEC variations caused by the ionosphere, for a location at $[25^\circ \text{ S}, 20^\circ \text{ E}]$ in South Africa on 2003-04-11 along azimuth $35^\circ$ and $25^\circ$ elevation. . . . .	54

21	Night time sTEC variation caused by the ionosphere, from a location at [25 <sup>0</sup> S, 20 <sup>0</sup> E] in South Africa on 2003-04-11 between 00H00 to 05H00 hours along azimuth 35 <sup>0</sup> and 25 <sup>0</sup> elevation. These values were derived using the extended Chapman profile.	55
22	Night time sTEC variation caused by the ionosphere, from a location at [25 <sup>0</sup> S, 20 <sup>0</sup> E] in South Africa on 2003-04-11 between 17H00 to 23H00 hours along azimuth 35 <sup>0</sup> and 25 <sup>0</sup> elevation. These values were derived using the extended Chapman profile.	56
23	vTEC derived from IRI 2001 data compared with <i>TEC</i> reconstructed from Fourier series using coefficients obtained from the IRI 2001 data on 2005-05-05 between 18H00 and 06H00 UT at <b>i-</b> HERM, <b>ii-</b> SUTH . . . . .	57
24	vTEC derived from IRI 2001 data compared with <i>TEC</i> reconstructed from Fourier series using coefficients obtained from the IRI 2001 data on 2005-05-05 between 18H00 and 06H00 UT at <b>i-</b> DRBN and <b>ii-</b> GEOS. . . . .	58
25	vTEC derived from IRI 2001 data compared with <i>TEC</i> reconstructed from Fourier series using coefficients obtained from the IRI 2001 data on 2005-05-05 between 18H00 and 06H00 UT at <b>i-</b> PBWA, and <b>ii-</b> KMAN respectively. . . . .	59
26	Diurnal sTEC variation at different longitudes from a location: [30 <sup>0</sup> S, 30 <sup>0</sup> E and 30 <sup>0</sup> S, 20 <sup>0</sup> E] on 2003-04-11 along azimuth 35 <sup>0</sup> and elevation 25 <sup>0</sup> . . . . .	61

27	Diurnal changes in differential sTEC longitudinal gradient caused by the ionosphere, from locations: [30° S, 30° E and 30° S, 20° E] on 2003-03-11 along azimuth 35° and elevation 25°. The sTEC gradient remains fairly constant between 07H00 and 14H00 hours. . . . .	61
28	Diurnal sTEC variation at different latitudes from locations; [30° S, 20° E and 20° S, 20° E] on 2003-04-11 along azimuth 35° and elevation 25°. . . . .	62
29	Predicted differential sTEC variation at constant baseline length for radio telescopes with East-West and North-South configuration on 2003-04-11 along azimuth 35°. Differential sTEC variation is not highly pronounced in the North-South configuration. . . . .	63
30	Predicted sTEC variation with elevation angles on 2003-04-11 along azimuth 35° from [25° S, 20° E]. . . . .	64
31	Snapshot [a 10 minute window] of the variation of sTEC derived from GPS observation data recorded at Hermanus dual frequency receiver station on 2003-04-11. . . . .	69
32	Fourier transform of sTEC derived from GPS data recorded at Hermanus dual frequency receiver station on 2003-04-11. The ftec is the FT of sTEC. There is no noticeable dominant frequency, indicating that the scintillations are absent. . . . .	71

33	Fourier transform of sinusoidal sTEC by a dominant Frequency of 0.01 Hz. This is an indication that the scintillations characterized by 0.01 Hz could be detected if they were present in the 10 minute snapshot GPS data recorded between 10H00 and 10H10 for a satellite at an elevation of $32.34^{\circ}$ . . . . .	72
34	Typical SKA ionosphere correction process. . . . .	77
35	Cartesian coordinates . . . . .	79
36	Geocentric and Geodetic coordinate system . . . . .	85
37	Right Ascension-Declination coordinate system . . . . .	89
38	Orbit orientation in $\alpha - \delta$ coordinate system . . . . .	90
39	Sidereal and Local Sidereal time . . . . .	92
40	Azimuth-Elevation Coordinate system. The position of the satellite (designated as object) is specified with respect to position of the observer coordinates.) . . . . .	94

## List of symbols and abbreviations

- $a$ : semi-major axis
- $A_{eff}$ : Effective aperture of the telescope
- $B$  : Baseline distance
- $\vec{B}$  : magnetic field vector
- $B_g$ : semi-minor axis
- $D$  : Declination of the radio antennas
- $b$ : semi-minor axis
- $E_x$ : The x component of the electric field.
- $e$  : Electron charge
- $f_1, f_2$ : Frequency of GPS signals
- $f_p$ : Plasma frequency
- $f_r$ : Fringe rate
- $HA$ : Hour Angle
- $h_c$ : Ellipsoidal height
- $h_m$ : Height at peak electron density
- $I_{fp}$ : Observed Intensity
- $L$ : Electron loss rate through recombination
- $mas$  : milliarcseconds
- $m_e$  : Electron mass
- $N_a$ : Number of antenna elements
- $N_e$ : Electron density
- $n$  : Complex refractive index
- $q_0$  : Peak electron production rate
- $S_{rs}$  : Radio Source structure index
- $t$  : Time in seconds
- $V(u, v)$ : True Visibility
- $V'(u, v)$ : Measured Visibility
- $V_{fp}$ : Spatial coherence function

- $V$ : Amplitude of fringe pattern
- $Z$ : Solar zenith distance
- $l, m, n$ : Direction cosines of the radio sources
- $u, v, w$ : The spatial, projected baselines
- $\Delta\tau_{ion}$ : Ionospheric delay
- $\Delta\phi_{obs}$ : Received differential phase at an interferometric unit
- $\delta$ : Declination of radio source
- $f$ : Frequency of an electromagnetic wave
- $f_c$ : Collision frequency of electrons in plasma
- $\theta$ : Angular separation between the magnetic field and Coulomb force
- $\theta_{ab}$ : Angular distance between radio wavefront and the baseline vector
- $\epsilon_0$ : Dielectric constant in vacuum
- $\Omega$ : Solid angle subtended by radio source
- $\Omega_e$ : Earth's rotation rate, [rads/sec]
- $\omega_B$ : gyro-frequency
- $\omega_s = B_\lambda \cdot S_0$ : Spatial frequency
- $\Phi_c$ : geographical latitude
- $\phi_d$ : Dispersive component of the phase delay
- $\phi_T$ : Total phase delay between radio antenna pair
- $\phi_r$ : Reference phase
- $\tau_g$ : Geometric signal delay
- $\tau_h$ : Hour angle

- $\tau_n$  : Frequency dependent signal delay
- $\psi_V$ : Visibility phase delay
- $\psi_m$ : Geomagnetic latitude
- $\Delta B$ : Radio antenna baseline offset
- $\Delta\phi_g$ : Geometric phase difference of a radio signal due to the path length difference between two radio antennas
- $\Delta\phi_s$ : Radio Source offset angle
- $\Delta\alpha$ : Right ascension offset
- $\Delta\delta$ : Declination offset
- $\theta_s$ : Separation angle between  $\vec{S}$  and  $\vec{B}$
- $\alpha$  : Right ascension of the radio source
- $\lambda$ : Wavelength of the radio signal
- GPS: Global Positioning System of satellites
- $TEC$ : Integrated Total Electron Content of the ionosphere
- $T_{sys}$ : System Temperature
- sTEC: Slant  $TEC$
- vTEC: Vertical  $TEC$
- SLIM: Single Layer Ionospheric Model
- TIDs: Travelling Ionospheric Disturbances
- IRI: International Reference Ionosphere
- SAST: South African Standard Time

# 1 Introduction

Radio signals from extra-terrestrial radio sources, (Radio Astronomy sources) received by two or more radio telescopes positioned on Earth propagate through the ionosphere and troposphere. The principle of interferometry, can be used to combine these signals to derive parameters that describe the structure of the radio sources, their celestial positions<sup>1</sup> as well as the medium through which these signals propagate and the positions of the receiving telescopes on the earth's surface. The envisaged SKA project with design specification given in Table 1 requires the forecasting of ionospheric conditions over each receiving antenna so as to correct for any errors in astrometric parameters, (e.g. radio source coordinates, radio source structure index<sup>2</sup>) caused by the ionosphere and derived from the astrometric observables such as the difference in arrival times of a wavefront at the receiving antennas, and the phase-delay rates, [Adam, 2003].

In this thesis, I have simulated and estimated phase delay resulting from ionospheric total electron content, ( $TEC$ ) and  $TEC$  variability along ray paths, from the target radio source to the receiving antennas and analyzed the influence these delays have on estimating the position of the radio source. Phase delay and phase changes are key parameters in radio astrometry<sup>3</sup>. A

---

<sup>1</sup>The position of the radio source is given in terms of the declination,  $\delta$  and hour angle ( $HA$ ).

<sup>2</sup>The radio source structure index ( $S_{rs}$ ) is a measure of the astrometric quality of the observed radio source.

<sup>3</sup>Astrometry deals with the determination of location, structure and motion of celestial objects, while astronomy deals the study of properties of individual and/groups of stars.

Table 1: Scientific specifications of Square Kilometer Array, [Taylor, 1999].

Parameter	Target Goal
$\frac{A_{eff}}{T_{sys}}, [m^2 K^{-1}]$	$2 \cdot 10^4$
Antenna spacing, [km]	1000-10,000
Number of stations	$\approx 1000$
Frequency range, [GHz]	0.15-20
Collecting area, [ $km^2$ ]	$\approx 1.0$
Angular resolution, [ $mas$ ]	0.1-0.001
Primary beam separation, at low frequency, [ $^\circ$ ]	100
Primary beam separation, at high frequency, [ $^\circ$ ]	1
Imaging field of view, at 1.4 GHz, [ $^\circ$ ]	1
No. of instantaneous beams	100
Brightness sensitivity, at 1.4 GHz, [K]	1
No. of spectral channels	$10^4$
No. of simultaneous channel frequency bands	2
Image dynamic range, at 1.4 GHz	$10^6$
Polarisation Purity, [dB]	-40

major goal of observational astronomy is to form images of the sky brightness distribution as a function of position, frequency, polarisation and time. Therefore obtaining the absolute position of the radio sources, to an accuracy of  $mas$  using centimeter wavelength techniques [Yusef-Zedeh et al, 1999] is required in radio astronomy.

To get an accurate position of radio astronomy sources and the images

of the radio sources, one approach is to use a calibrator i.e a reference radio source close to the target source and observe the two radio sources alternately while measuring the received signal at two or more antennas, (phase referencing). But this does not correct absolutely the effects that the ionosphere causes on the radio signals because the switching time interval between the target radio source and the calibrator is of the order of minutes. Ionospheric conditions change in much smaller timescales, ( $t < \text{minutes}$ ) and therefore, absolute correction for the effects of the ionosphere on radio signal propagation cannot be achieved. Phase referencing is also not suitable for imaging weak radio sources. Other techniques that have been proposed include, fast frequency switching [Middelberg et al, 2005] and post delay analysis. These techniques also have weaknesses. A good model of ionospheric  $TEC$  variability is needed in order to correct for the errors induced on estimating the phase difference between the calibrator and the target source. Data obtained from GPS satellites can be used to derive ionospheric parameters that could be used to correct for the phase delay within shorter timescales, (in seconds) crucial for ionospheric now-casting required for radio-astronomy.

The ionosphere's effect on radio astrometric observables in radio astronomy is frequency dependent. The dependence is related to the number of electrons in the ionosphere which is numerically expressed as:

$$N(m^{-3}) = 1.24 \times 10^{10} [f(MHz)]^2 \quad (1)$$

This can be rewritten in terms of the plasma frequency,  $f_p$ , as

$$f_p \approx 9\sqrt{N_e} \quad (2)$$

Here,  $N_e$  is the electron density in  $m^{-3}$  and  $f$  is in hertz, (Hz). A change

in the refractive index within the ionospheric medium causes a change of the phase and group velocities of a radio signal along the propagation path [Perley and Bust., 2002], in the ionosphere relative to the velocity of the electromagnetic wave in free space. The delay in phase velocity relative to free space propagation in turn causes a time delay of the coded radio signal propagating through the ionospheric medium. In this thesis, I describe and present the simulated, (from the Chapman profile) and measured, (from GPS data) ionospheric  $TEC$  and  $TEC$  variability, over the proposed SKA sites. The interaction of extra-terrestrial radio waves with the ionosphere will be discussed in section two. In section three,  $TEC$  variability will be presented. Ionospheric correction techniques, suitable for the SKA will be described in section four. In section five, simulated results of the errors in the positioning of astronomical radio sources resulting from  $TEC$  and  $TEC$  variability will be presented. Finally, some conclusions will be drawn based on the simulated and measured results.

## 2 Ionospheric Interactions with extra-terrestrial radio waves

### 2.1 Introduction

The ionosphere modifies the polarisation, angle of arrival and the phase and amplitude of transionospheric radio signals [Perley and Bust., 2002]. This modulation is pronounced at frequencies,  $f < 10$  GHz. For a single element interferometer<sup>4</sup>, this effect might not be captured, i.e an interferometer is sensitive to total phase perturbation. Typical ionospheric effect parameters are given in Table 2.

Table 2: Ionospheric perturbations for a column density of  $10^{17} \frac{\text{electrons}}{\text{m}^2}$

Characteristic	Typical perturbation value (100 MHz)
Phase-path length	-400 [in meters]
Phase change	-840 [in radians]
Refraction	1.3 [arc-minutes]
Polarisation Rotation	6.6 [radians]

For an  $N_a$ -array of antenna elements, the ionospheric effect on a phase-path change at each pair of stations, which are connected by a baseline vector,

---

<sup>4</sup>*An interferometer is sensitive to differential phase variation, which can be reconstructed from the difference in integrated electron densities along ray paths to the two receiving stations that form an interferometer unit.*

can be determined from the differential  $TEC$ , (the difference in integrated total electron content along each path length from the radio source to an interferometer pair) between the stations.

Predicting and estimating the phase perturbations of the ionospheric medium on radio signals (as would be measured at the proposed sites of the SKA antennas) can be used to determine parameters that relate to the positioning and imaging of radio sources. Ionospheric perturbations are derived from the parameters that describe the interactions of the extra-terrestrial radio signals with the ionosphere. Measurable changes in the phase, amplitude, and polarisation of the extra-terrestrial radio signals can be used to infer conditions within the ionospheric medium. In this section, I will discuss interactions of the radio waves with the ionosphere, and derive the relationship between the phase delay and the refractive index.

## **2.2 Radio signal interactions with ionosphere**

The upper atmosphere is said to be a 'magneto-plasma' due to the presence of the geomagnetic field. The properties of an electromagnetic wave traversing such a medium is therefore based on the magneto-ionic theory [Budden, 1985]. The electromagnetic wave passing through the ionosphere is governed by the Appleton-Hartree equation given in (3).

$$n^2 = \frac{X}{1 - jZ - \left( \frac{Y_T^2}{2(1-X-jZ)} \right) \pm \left( \frac{Y_T^4}{4(1-X-jZ)^2} + Y_L^2 \right)^{\frac{1}{2}}} \quad (3)$$

Here,  $n$  is the complex refractive index, the  $\pm$  show the ordinary, (+) left-hand circularly polarized mode and extra-ordinary, (-) mode, which is right-hand circularly polarized, since the ionosphere is a bi-refringent medium and;

$$X = \frac{f_p^2}{f^2} \quad (4)$$

$$Y = \frac{\omega_{\vec{B}}}{f} \quad \text{which has components} \quad (5)$$

$$Y_L = \frac{\omega_B \cos \theta}{f} \quad (6)$$

$$Y_T = \frac{\omega_B \sin \theta}{f} \quad (7)$$

$$Z = \frac{f_c}{f} \quad (8)$$

where,  $X$  accounts for the thermal motion of the electrons,  $Y_L$  accounts for the Lorentz force due to the interaction of the electron with the magnetic field,  $Y_T$  is the transverse component of the Lorentz force,  $f_p = \sqrt{\left( \frac{N_e e^2}{\epsilon_0 m_e} \right)}$  and  $\omega_B = \frac{\vec{B}e}{m_e}$  are the plasma and electron gyro-frequency respectively, for which  $e$  is the electron charge,  $\vec{B}$  is the magnetic field vector and  $m_e$  is the mass of the electron.  $f_c$  and  $f$  are the electron collision frequency and radio wave frequency respectively while  $\theta$  is the angle between the direction of propagation and that of the geomagnetic field. The terms  $X$ ,  $Y_L$ ,  $Y_T$  and  $Z$  are dimensionless quantities that describe the motion of free electrons in the ionosphere.

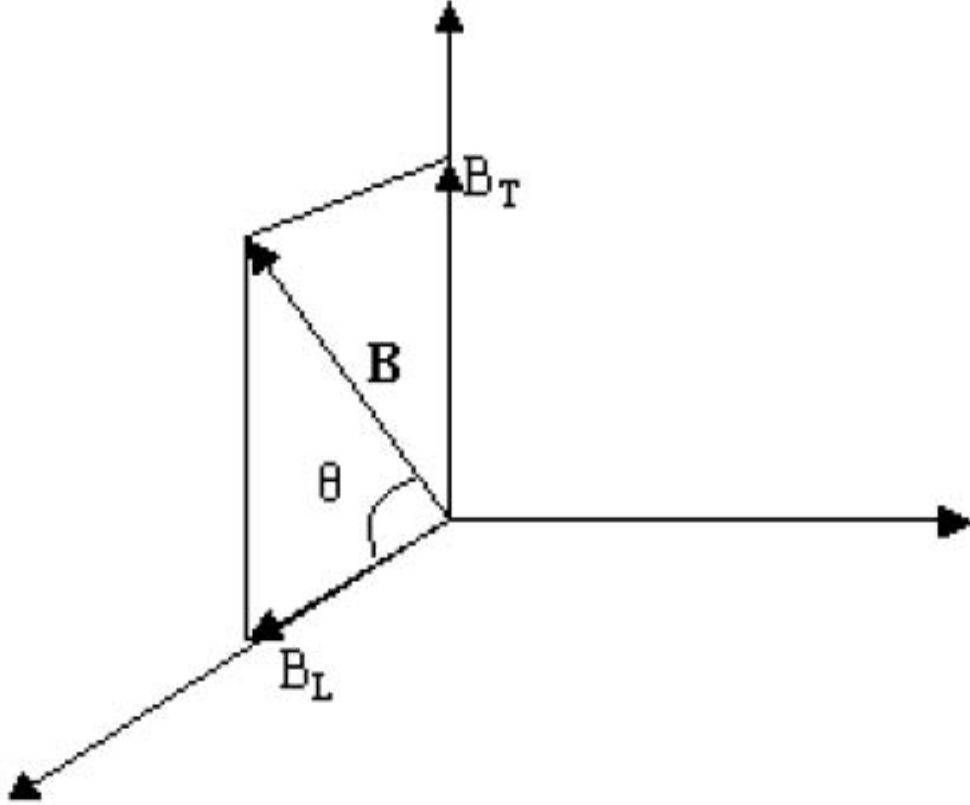


Figure 1: Magnetic field  $\mathbf{B}$  inclined  $\theta^0$  with the z-axis. The Transverse of Lorentz force is ignored at much higher frequencies.

If the collision frequency is ignored, ( $Z=0$ , for a cold plasma approximation), Equation (3) becomes,

$$n^2 = 1 - \frac{2X(1-X)}{2(1-X) - Y^2 \sin^2 \theta \pm [Y^4 \sin^4 \theta + 4Y^2 \cos^2 \theta (1-X)^2]^{\frac{1}{2}}} \quad (9)$$

At frequencies much higher than the gyro-frequency of electrons/ions (i.e  $f \gg \omega_B$ ),  $Y$  can be ignored since at this high frequency the electrons/ions

do not feel the effects of the magnetic field, (the 'fixed in' concept is violated) and Equation (9) reduces to:

$$n^2 \approx 1 - X = 1 - \frac{f_p^2}{f^2} \quad (10)$$

where,  $f_p$  is the plasma frequency and  $f$  is the frequency of the electromagnetic wave propagating through the plasma. The approximation given in Equation (10) shows that, for a radio wave propagation, the ionosphere has a dielectric constant less than unity. Equation (10) can be Taylor expanded and written as;

$$n \approx 1 - \frac{f_p^2}{2f^2} \quad (11)$$

Equation (11) can be re-written in terms of the delay that the signal experiences due to its propagation through the ionosphere of length,  $L$ , normalized by the speed of light. Thus, the ionospheric delay can be written as

$$\Delta\tau_{ion} = \frac{\int_0^L (n - 1) dl}{c} \quad (12)$$

This delay is part of the total delay measured by a two-element interferometer discussed in Chapter four. Substituting Equation (11) into Equation (12) yields:

$$\Delta\tau_{ion} = -\frac{\int_0^L f_p^2 dl}{2c \cdot f^2} \quad (13)$$

where,  $f_p \approx 9\sqrt{N_e}$  [ Hz] and  $N_e$ , [ $\frac{electrons}{m^3}$ ] is the electron density of the ionosphere. Equation (13) now becomes:

$$\Delta\tau_{ion} = \frac{-40.5 \cdot \int_0^L N_e dl}{c \cdot f^2} \quad (14)$$

Since,  $TEC = \int_0^L N_e dl$ , Equation (14) can also be expressed as:

$$\Delta\tau_{ion} = \frac{-40.5 \cdot TEC}{c \cdot f_p^2} \quad [\text{seconds}] \quad (15)$$

where,  $TEC$  is the total electron content in  $[\frac{electrons}{m^2}]$ ,  $c$  is the speed of light  $[\frac{m}{s}]$  and  $f_p$  is in Hz. This can be further converted to phase delay  $\Delta\phi_{ion}$ ;

$$\begin{aligned} \Delta\phi_{ion} &= [\Delta\tau_{ion}] \cdot 2\pi f_p \\ &= \frac{-8.4832 \cdot 10^9 \cdot TEC}{f_p} \quad [\text{in radians}] \end{aligned} \quad (16)$$

here,  $TEC$  is expressed in total electron content units (TECU), and 1 TECU =  $10^{16} \frac{electrons}{m^2}$ .

In this thesis, I have focused on the phase delay; a dispersive component causing a delay which is ionospheric, and frequency dependent. In the next section, I will describe various parameters that are used to characterize the ionosphere.

### 2.3 Characterising the ionosphere

The sun's radiation causes ionization in the ionosphere, with a height range  $\approx 50$ -2000 km, [Gao and Liu., 2002]. This produces free electrons which, from a height of 50 km, advance or delay the radio waves. Ions are also produced, and the number of electrons and ions are nearly equal <sup>5</sup>. The spatial distribution of these charged particles is due to photochemical and

---

<sup>5</sup>The ionosphere is a quasi-neutral medium, [Milan, 2004].

transportation processes. These processes distribute the ionic species at different heights. The regions formed are labelled depending on the type of the dominant ionic species. The E-region is dominated by  $O^{2+}$  ions,  $NO^+$  dominate the F1 region while  $O^+$  dominate the F2. The topside, extending from the F2 layer is characterized by decreasing  $O^+$  ions as  $H^+$  and  $He^+$  become dominant.

The absorption of solar radiation as it passes through the ionosphere, decreases with decreasing height (measured from the surface of the earth). This implies that there is less ionization, and thus a lower concentration of electrons with increase in height per square meter as depicted by the general Chapman profile [Budden, 1985] and [Stanimir et al, 2003] given in Equation (17) and shown in Figures 2 and 3,

$$N_e(h) = N_e(h_m)e^{(k[1-Z-e^{-Z}])} = N_e e^{1-Z-\sec \chi e^{-Z}} \quad (17)$$

where,  $h_m$  is the height at peak density,  $N_e(h_m)$ . If  $q_0$  is the peak production rate, ( $m^{-3}s^{-1}$ ), and  $\alpha$  the recombination rate ( $m^3s^{-1}$ ), the peak density is given by  $N_e(h_m) = \sqrt{\frac{q_0}{\alpha_{rec}}}$ .  $Z$  is given in terms of the scale height ( $H$ ) given by Equation (18).  $\chi$  is the parameter defining the solar zenith angle dependence of the Chapman layer.

$$Z = \frac{h - h_m}{H} \quad (18)$$

Here,  $H = \frac{h-50}{3}$ , and we have,

$$h_m = h_{min} + \frac{50}{2} [1 + \cos \xi] \quad (19)$$

$$\text{where } \xi \approx 0.001[\sin(\psi_m + \frac{HA}{2})] \quad (20)$$

Here,  $h_m$ ,  $[270 \leq h_m \leq 450, \text{ km}]$  depends on the hour angle,  $\tau_h$  and the geomagnetic longitude,  $\psi_m$  is the mean intersection of the ray path and the ionosphere layer for a particular elevation, azimuth, longitude and latitude of the observing station. The coefficient,  $k$  represents the two distinct formulations, dependent on the photochemical process in play, as described below:

**$\alpha$ -Chapman,  $k=0.5$**  - This assumes that the electrons recombine directly with positive ions,  $X^+ + e \rightarrow X$ . The number of electrons available is negligible. The loss rate is given by,  $L = \alpha_{rec}N^2$ . Here,  $\alpha_{rec}$  is the recombination rate. I have considered this mechanism since the ionospheric electron density variation has a quadratic form.

**$\beta$ -Chapman,  $k=1$**  - Here, the electron loss is through attachment to neutral particles,  $X + e \rightarrow X^-$ . The loss rate is linear and is given by,  $L = \beta_{at}N$ . Here,  $\beta_{at}$  is the attachment coefficient. This process is associated with electrons in the D-region.

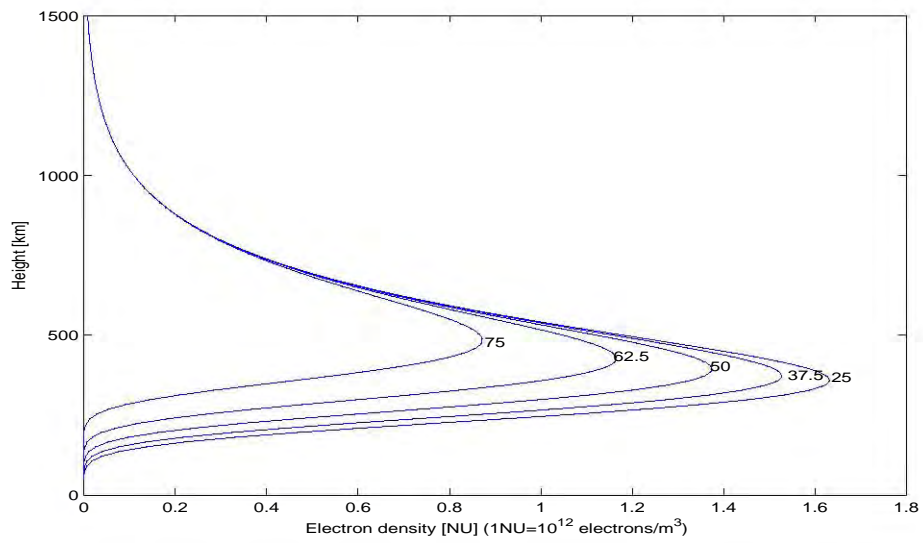


Figure 2: The  $\alpha$ -Chapman profile for the vertical electron density variation. The loss mechanism is through direct attachment to positive ion species. The different curves depict the effect of solar zenith angle, in degrees, on total electron densities in the ionosphere.

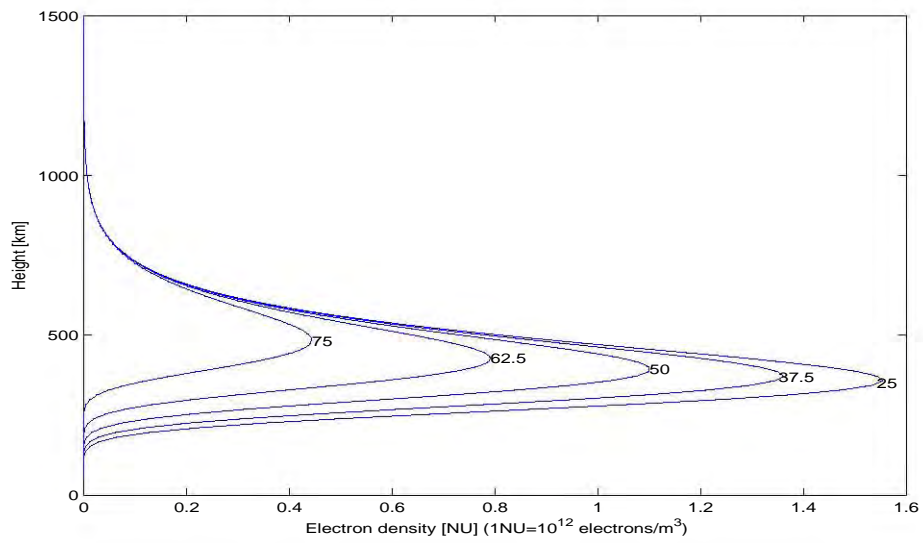


Figure 3: The  $\beta$ -Chapman profile for the vertical electron density variation. The equilibrium condition is affected by loss of electrons through attachment to neutral molecules. The different curves show the variation of electron density in the ionosphere with solar zenith angle in degrees.

The degree of ionization is a balance between the rates at which the electrons/ions are produced and lost. The production and loss rates in turn depend on the concentrations of the different gases in the atmosphere. The production rate of the ions/electrons depend also on the intensity and wavelength of the radiation from the sun. The ionosphere remains quasi-neutral due to an equilibrium state between the production and loss of the ions/electrons.

The state of equilibrium of charged particles varies with height in the ionospheric medium. This leads to the medium exhibiting layers, manifesting degrees of ionization. These layers are characterized by differing density of electrons/ions. The degree of ionization is dependent on the temperature of particles present. In this way, the ionospheric medium is layered into regions. The regions of the bottomside ionosphere are shown in Figure 4 and described as:

**D-region** - This is the lowest ionospheric layer covering an altitude of about 60-90 km. Hard X-rays and solar Lyman radiation ionize the molecules which in turn absorb the radio signals with frequencies in the lower VHF band.

**E-region** - This region is in the height range, 90-140 km. Ionization here is due to soft X-rays. Scintillations are often observed in this region due to solar particle precipitation in the aurora region.

**F1-region** This layer lies between 140-210 km. It is only observed during the day. It is more pronounced during summer than winter and during ionosphere storms, [Davies, 1990].

**F2-region** This has a characteristic height of 200-400 km. It is the most dense of the regions and exhibits the highest variability with height fluctuating between 250-450 km. It is mainly produced from ionization of atomic oxygen which is the main constituent at this height.

The topside ionospheric layer starts at the F2 peak layer height and extends to about 3500 km, [Bilitza et al, 1998].

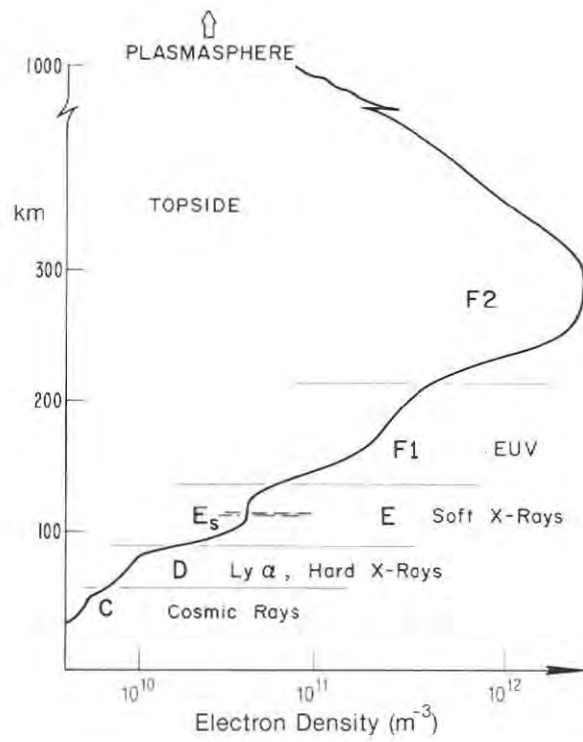


Figure 4: Mid-latitude ionosphere structure during the summer day. Main ionizing radiations are indicated. Taken from Davies [1990].

Another aspect of characterising the ionosphere is by monitoring the variation of  $TEC$  along a ray path through the ionosphere from the D-region to the topside of the ionosphere. If the ray path is in the solar zenith direction, vertical  $TEC$  (vTEC) is computed, otherwise slant  $TEC$  (sTEC) is determined. vTEC can be computed from sTEC using a single layer (SLIM) mapping function or the obliquity factor given by Equation (21).

$$F(z) = \frac{1}{\cos z'} \quad \text{where} \quad (21)$$

$$\sin z' = \frac{R_e}{R_e + H_{io}} \sin z$$

Here,  $R_e$  is the mean earth radius while  $H_{io}$  is the ionospheric height above the surface of Earth in km.

The slab thickness; the depth of an imaginary ionosphere with the same  $TEC$  as the actual ionosphere and with uniform electron density equal to the maximum electron density of the actual ionosphere [Goodwin, 1995] can also be used to describe the vertical variation of electron density in the ionosphere. In the next section, monitoring and estimating total electron content variability using Chapman profile, IRI and GPS data will be discussed.

## 3 Total Electron Content (*TEC*) Variability

### 3.1 Introduction

The *TEC* over a specific region of the Earth does not remain constant throughout the year, month, day and even hour. Observations of the ionosphere at smaller time scales reveal transient variations. A number of physical processes have been suggested as being the cause of these spatial and temporal variations. Aurora and solar events cause variations in time scales of seconds to hours. Atmospheric temperature and pressure changes are evident in the ionospheric variations since the ionosphere is coupled with the lower atmosphere. Variations of the magnetic, (during magnetic storms and sub-storms) and electric fields induce variations in the parameters that characterize the state of the ionosphere. The ionosphere nearly (there are subtle lags) co-rotates with the Earth, (since the ionospheric electrons are fixed into the earth's magnetic field) so ionospheric variations may show an imprint of irregular motion of the earth. Therefore, accurate monitoring of fast changes will depend on the type of ionospheric model, i.e. it's ability to resolve changes at smaller time scales. In the next section, I will describe the temporal variations of *TEC*.

### 3.2 *TEC* Variability

The effects that an ionospheric medium induces on the radio signal passing through it have been under continuous investigation. The nature of the ionosphere is well understood. A number of empirical [Brunner, 1991]

and [Klobuchar, 2001] and physical models [Bilitza, 2003] for ionospheric characterization have been suggested. The main area of concern to radio astronomers is the disturbances that the ionosphere causes to extra-terrestrial radio signals propagating through it. These disturbances can be described in terms of *TEC* variability. The measured variability is caused by atmospheric wave motions and plasma dynamics through electrodynamic processes. For instance, the ionospheric wind dynamo generates electric fields which cause plasma drifts which are known to cause the equatorial electron density anomaly [Richmond, 1995]. The atmospheric gravity waves and the strong electric fields give rise to plasma density gradients which in turn cause electron density instabilities manifested in the form of *TEC* variations. Regular <sup>6</sup> and irregular <sup>7</sup> *TEC* variations have been observed. Below, I will describe some forms of regular variations.

**Diurnal Variations** - The ionospheric electron density exhibits regular variations, with a peak during the day to a minimum during the night. The F layer densities peak at about 14H00, South African Standard Time, (SAST). During early morning (04H00 to 07H00) and pre-dawn (18H00 to 20H00), the ionospheric densities can drop by two orders of magnitude. There are localized enhancements of these variations at late afternoon/evening. These temporal variabilities are however latitude and altitude dependent.

**27-Day and sun spot (SS) cycle variation** - As the sun rotates on its axis, the visibility trend of SS, follows the rotational period of the

---

<sup>6</sup>*Show uniform pattern, i.e. occur in cycles and are easily predicted.*

<sup>7</sup>*Arise due to abnormal behavior of the sun, and cannot be predicted easily.*

sun. The solar cycle (11 year cycle) is characterized by the intensity of the SS number, with increased SS at solar maximum while fewer SS occurring at solar minimum. The degree of ionization for each layer in the ionosphere varies with the 27-day solar variation as well as the 11 year solar cycle thus, the SS is a good measure of solar activity.

**Seasonal Variations** - These variations arise due to revolution of the earth around the sun. The relative position of the sun with respect to a point on the atmosphere/earth therefore varies. This means that there will be varying radiation at different locations on the earth's surface.

### **3.3 Methods of estimating *TEC* variability**

A number of methods have been used to compute *TEC* and *TEC* variability. The appropriateness of any given method depends on the application and type of data available. Empirical methods rely on observed data while physical models rely on profilers, from which *TEC* computation is based on predictions. *TEC* computed from GPS, VLBI, and international reference ionosphere, IRI, data have been used to compute *TEC* and *TEC* variability [Ciraolo and Spalla., 2002], [Kondo, 1991] and [Mamoru et al, 2003]. In this thesis, GPS data, model data and IRI 2001 data were used to compute *TEC* over the Southern African region. Figure 5 shows night time variation of vTEC computed from GPS data recorded by the Simonstown [34.19<sup>o</sup> S, 18.44<sup>o</sup> E] GPS receiver, predicted vTEC using model function and IRI 2001 data on 2003-03-13. The correlation indices between GPS(University of New Brunswick model, (UNB)) derived vTEC and model values and vTEC

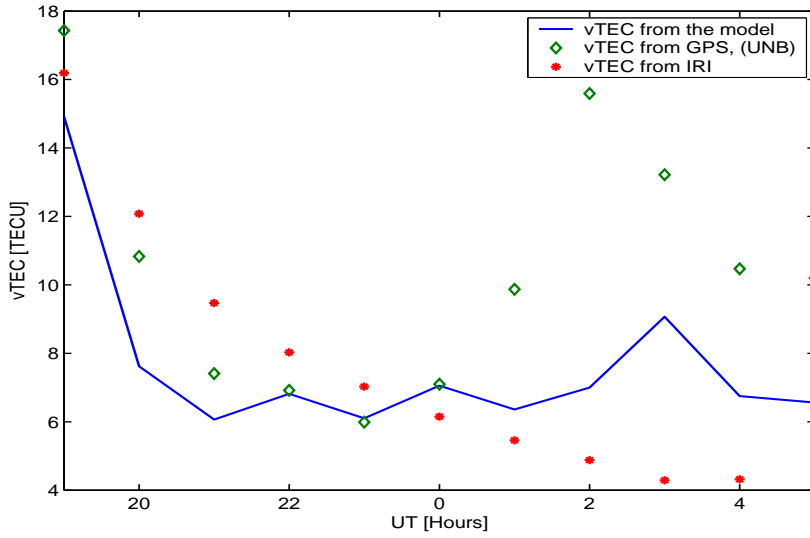


Figure 5: Night time IRI 2001, Model function, and GPS based vTEC at Simonstown,  $[33.19^{\circ} \text{ S}, 18.44^{\circ} \text{ E}]$  location on 2003-03-13.

derived from IRI 2001 and model vTEC are 0.9 and 0.8 respectively. This implies the level of agreement between model vTEC, GPS derived vTEC and vTEC derived from IRI 2001 is remarkable. The vertical *TEC* (vTEC) derived from GPS sTEC, from IRI 2001 data and the model function show similar pattern during night time. The IRI 2001 model computes average vTEC over a long timescale and therefore smears out temporal variations seen from GPS data and model function.

I have used the Chapman profile as presented by Feltens, (1998) to derive sTEC along a ray path at  $20^{\circ}$ , and  $35^{\circ}$ ; elevation and azimuth angles from an arbitrary chosen location,  $[25^{\circ} \text{ S}, 20^{\circ} \text{ E}]$ . Figure 6 shows the diurnal variation of the solar solar zenith angle.

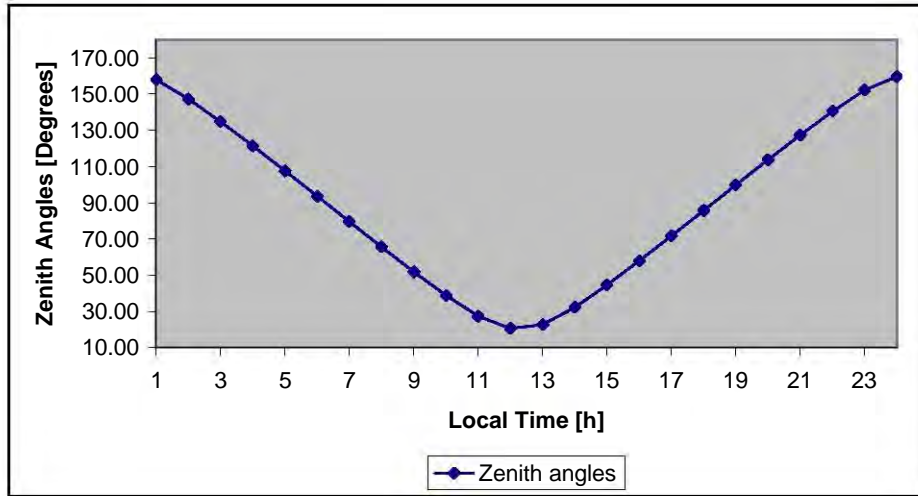


Figure 6: Variation of sun Zenith angle from [25° S, 20° E] on 2003-04-11.

However *TEC* dependence on solar zenith angle is not well explored in Feltens (1998). If the solar zenith angle is set to different values, night time *TEC* remains constant throughout but varies with these values as shown in Figure 7. It is evident that setting the solar zenith angle to a constant value at night does not depict the true nature of the ionosphere.

Instead of fixing the solar zenith angle, I have modelled the ionosphere using IRI 2001 data in two ways. First, *TEC* derived from the IRI 2001 data corresponding with solar zenith values greater than 89° (as shown in Figure 6 was fitted into a Fourier series. I have assumed that since solar zenith angles depend on time, a periodic function can represent the variability of the ionosphere during night time. A Fourier series of the form shown in Equation (22) was used.

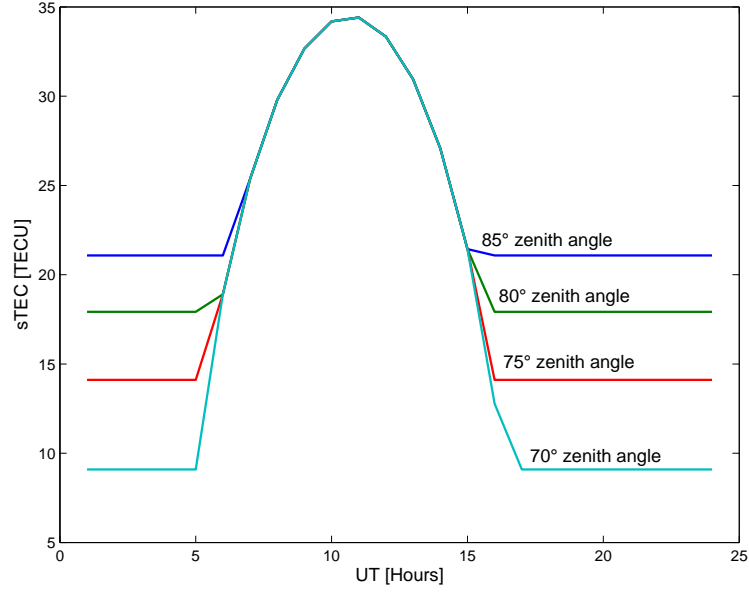


Figure 7: Diurnal  $TEC$  derived from the Chapman profile from  $[34.24^{\circ} \text{ S}, 19.26^{\circ} \text{ E}]$  on 2005-05-05. The solar zenith angles are fixed to  $70^{\circ}$ ,  $75^{\circ}$ ,  $80^{\circ}$ , and  $85^{\circ}$ .

$$g(z) = \frac{a_0}{2} + \sum_{l=1, z}^{l=3} a_l \cos(lz) + \sum_{l=1, z}^{l=3} b_l \sin(lz) \quad (22)$$

Here,  $l$  is the order of the Fourier series,  $a_0$ ,  $a_l$  and  $b_l$  are the coefficients of the function while  $Z$  is the azimuth angle. The coefficients were determined and used to estimate  $TEC$  during the night.  $TEC$  values computed in this way were then compared with night time  $TEC$  derived from IRI and shown in Figure 8a and b. The difference in the standard deviation between IRI derived  $TEC$  and  $TEC$  derived from the Fourier series is 2.2 TECU. The results show a similar pattern.

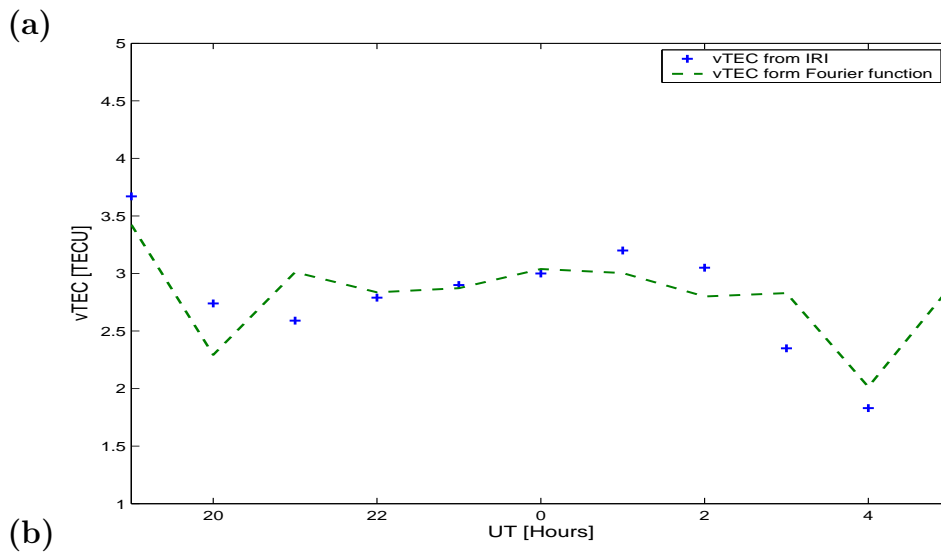
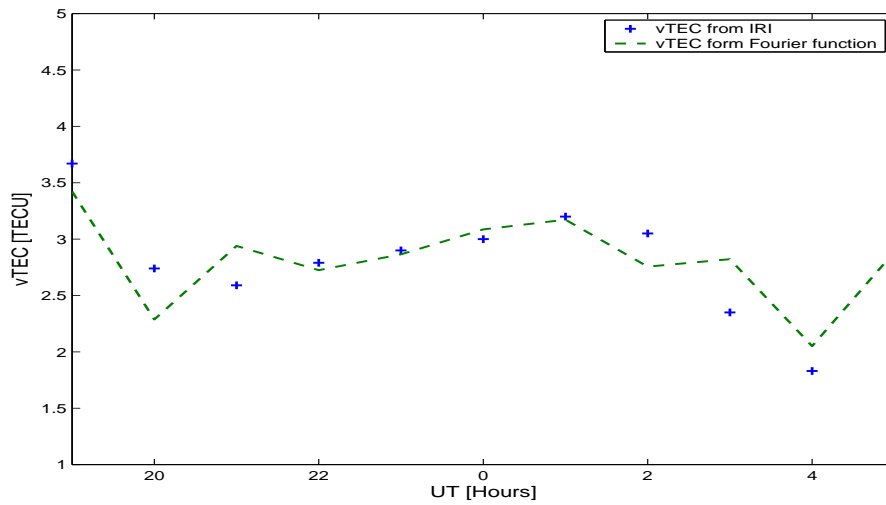


Figure 8: vTEC derived from IRI 2001 data compared with  $TEC$  reconstructed from Fourier series. Figure 8(a) shows the diurnal variation on 2001-03-14 while Figure 8 (b) shows variations on 2005-03-14. These results were calculated from a location with geographical coordinates,  $[34.22^{\circ}$  S,  $19.24^{\circ}$  E].

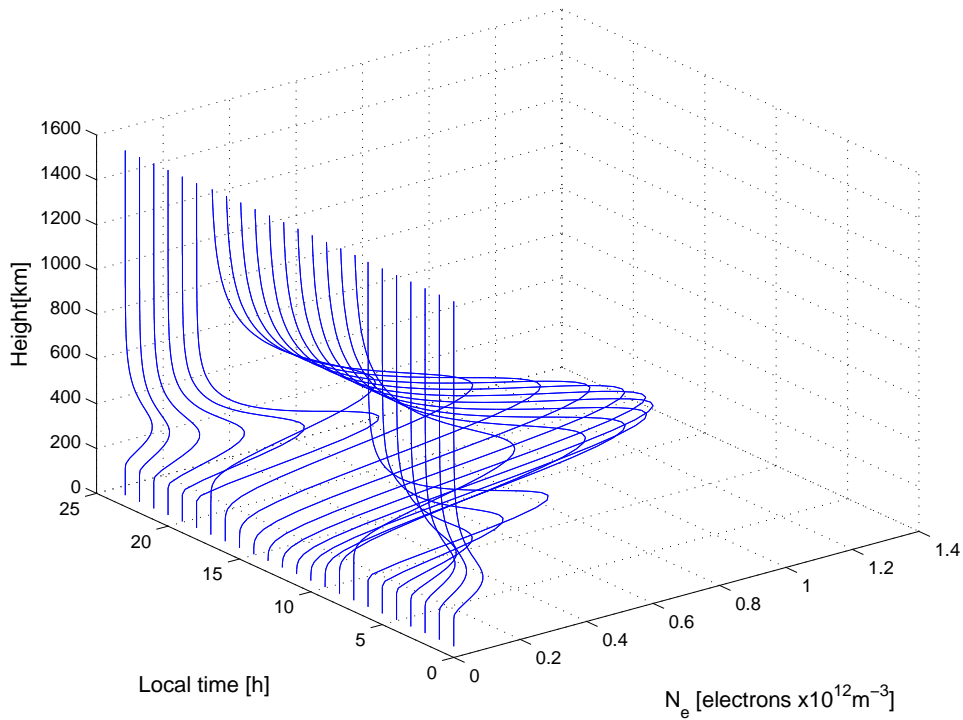


Figure 9: Electron density profiles derived using the on-line IRI 2001 model on 2003-04-11 for a location at  $[30.0^{\circ} \text{ S}, 20.0^{\circ} \text{ E}]$  along  $20^{\circ}$  and  $35^{\circ}$  elevation and azimuth angles respectively. Figure by Cilliers, [2005].

In the second approach, I have used a model by Cilliers, [2005] for vertical electron density profiles. This model is useful since it can be used to estimate night time *TEC* as opposed to the approach of the Chapman profile model. IRI 2001 data of 2003-04-11 was used to derive values of maximum  $N_e$  and *TEC* from each profile, see Figures 9 and 10.

A polynomial fit of  $N_e(\text{max})$  versus solar zenith angle was obtained for the night-time hours 18H00 to 06H00. Night time *TEC* values were determined

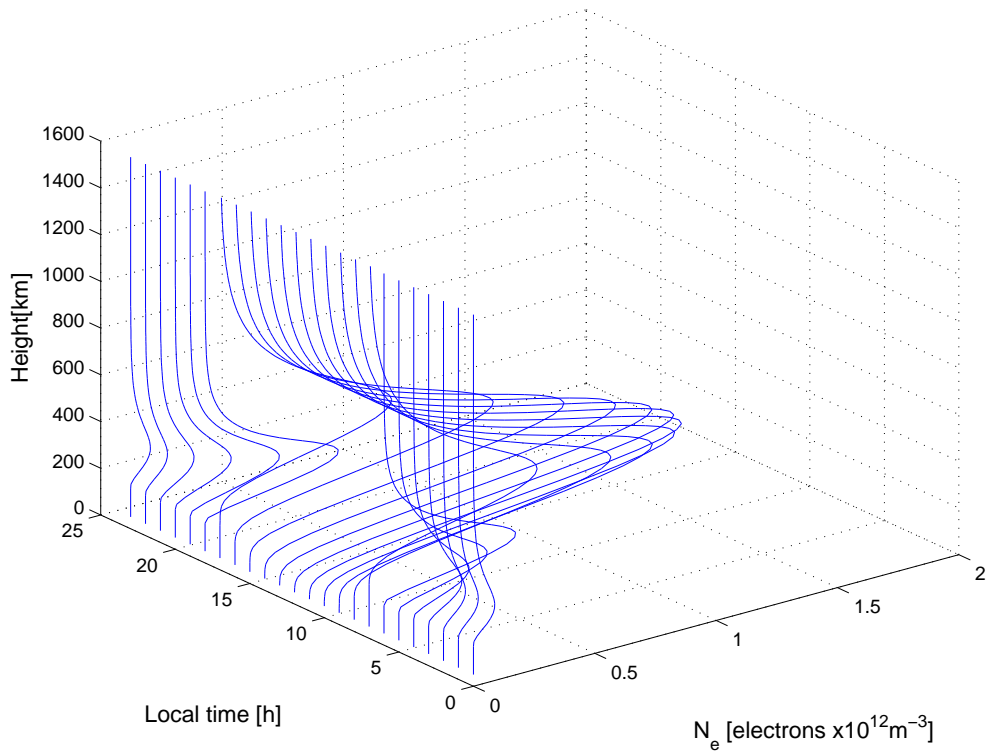


Figure 10: Electron density profiles derived using the extended Chapman profile on 2003-04-11 for a location at [30.0<sup>0</sup> S, 20.0<sup>0</sup> E] along 20<sup>0</sup> and 35<sup>0</sup> elevation and azimuth angles respectively.

using a skewed cosine profile (we now call the extended Chapman) with the same peak value as the polynomial approximation of  $N_e(\max)$  for night-time electron densities. The skewed cosine function is given in Equation (23). The IRI  $TEC$  values were compared to the Chapman and extended Chapman model. The extended Chapman model can be described as:

$$\begin{aligned} N_e &= N_m [1 - \cos \beta] \\ \beta &= 2\pi(1 - e^{-4h_z}) \\ h_z &= \frac{h - h_{min}}{h_{max} - h_{min}} \end{aligned} \tag{23}$$

Here,  $h$  is the height of the profiles,  $h_{min}$  is the minimum height of the ionosphere at night time,  $h_{max}$  is the maximum height of the ionosphere.  $N_m$  is the model electron density computed as follows;

$$N_m = \frac{1}{2} [\text{polyval}(p1, \psi \cdot 180/\pi)]; \tag{24}$$

where  $p1 = [0.0001 \quad -0.0312 \quad 2.5012]$  are the polynomial coefficients for night-time peak electron density fit to Solar zenith angles ( $\psi$ ) above  $85^\circ$ . These equations were implemented using Matlab, which has an in-built function 'polyval'. The relationship between peak electron density and solar zenith distances is shown in Figure 11.

Figure 12 shows the predicted pattern of  $TEC$  at night time using a Fourier series function and the polynomial function compared to  $TEC$  derived from IRI data on 2005-03-11.

Both models show a good correlation and can be combined to estimate empirical  $TEC$  values during the day and night time as opposed to the

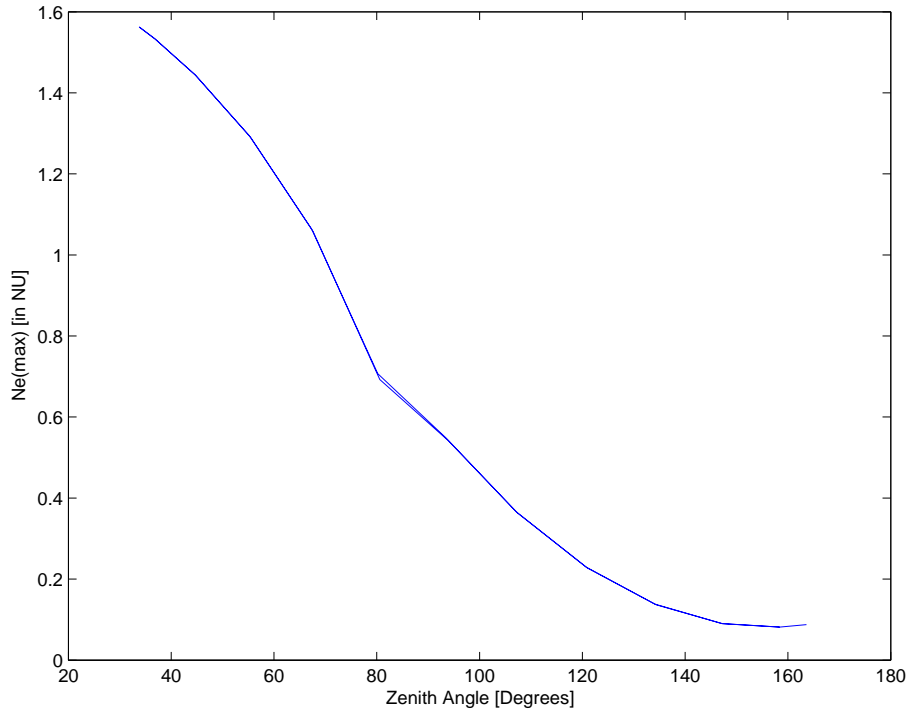


Figure 11: Derived peak electron density versus solar zenith angles as predicted from  $[25^{\circ} \text{ S}, 20^{\circ} \text{ E}]$  along  $20^{\circ}$ , and  $35^{\circ}$  elevation and azimuth angles respectively on 2003-04-11.  $1\text{NU}=10^{12} \frac{\text{electrons}}{\text{m}^3}$ . These are two curves but are superimposed to give the variation over a complete day.

Chapman profile.

A measure of  $TEC$  variation can be used as an indicator of a disturbance that the ionosphere imposes on a radio signal propagating through it. This measure is critical for radio astronomy observations. For effective evaluation of SKA astrometric performance, the ionospheric disturbance on the expected extra-terrestrial radio signals must be estimated. I have assumed that the radio receiving antennas will use an interferometric response and it

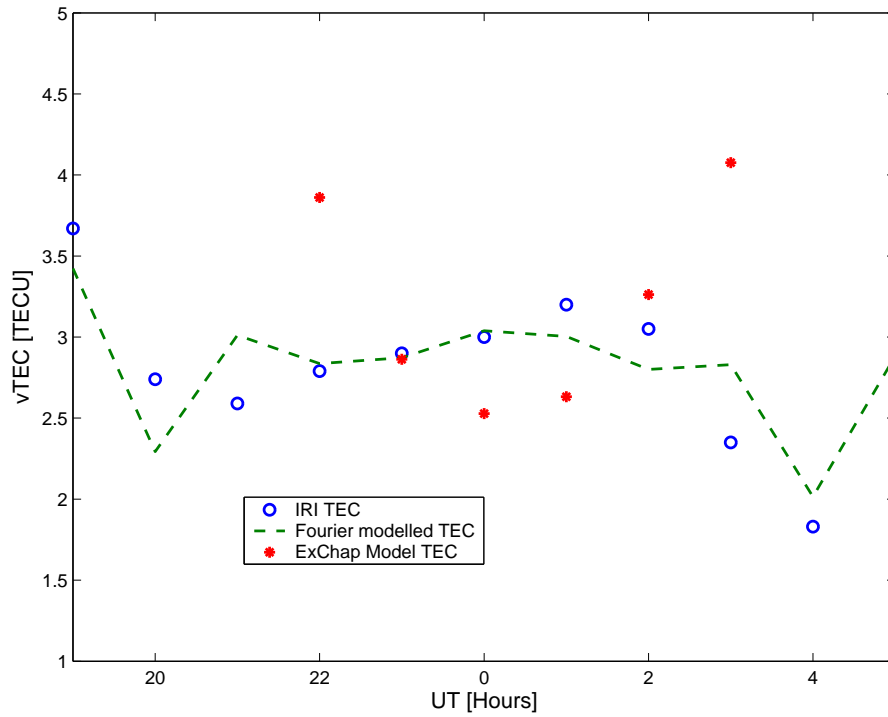


Figure 12: Night time  $vTEC$  computed from IRI 2001, the Fourier function as well as extended Chapman function. The Fourier function and the extended Chapman function use coefficients derived from the IRI 2001 data.

is from this response function that the signal components arising from the ionosphere, the atmosphere, baseline, source position and structure offsets could be reconstructed. In the next section, correction techniques for ionospheric disturbances are discussed, which are relevant to the SKA.

## 4 Ionospheric Correction Techniques, suitable for the SKA

### 4.1 Introduction

The basic principle of astrometry relies on the interferometric delay observable derived from observables of an interferometer response [Kaplan, 1998]. The response function is in turn the spatial coherence function<sup>8</sup> ( $V_{f_p}$ ), of the electric field between pairs of antenna elements located on the surface of the earth and at positions linked by a baseline vector,  $\vec{B}$ .  $V_{f_p}$  is related to the observed intensity,  $I_{f_p}$  from an astronomical point or extended radio source<sup>9</sup> in the direction  $\vec{S}$  given by Equation (25).  $V_{f_p}$  is measured in spectral power density units, ( $Wm^{-2}Hz^{-1}$ ) while  $I_{f_p}$  is measured in  $Wm^{-2}Hz^{-1}$ . The flux density is measured in Jansky, (Jy)<sup>10</sup>.

$$V_{f_p}(\vec{B}) = \int_{sky} I_{f_p}(\vec{S}) e^{\frac{-2\pi i \omega \vec{S} \vec{B}}{c}} d\Omega \quad (25)$$

where,  $\Omega$  is the solid angle formed by the radio source.

---

<sup>8</sup> $V_{f_p}$  is a complex quantity and is also called the visibility function.

<sup>9</sup>A point source is an idealized source which subtends a very small angle. An extended radio source emit radiations that cover a large part of the sky, e.g. the Milky way galaxy, and its galactic center, Sagittarius A.

<sup>10</sup> 1 Jy =  $10^{-26} Wm^{-2}Hz^{-1}$ .

## 4.2 An Interferometer receiver system

An interferometer receiver system consists of feed, amplifier and mixers  $M_1$  and  $M_2$  all arranged in a particular pattern to minimize instrumental biases. The received signal is used to reconstruct the structure and position of radio sources in the sky. The signal measured is (the sampled version which yields the dirty map [Haniff, 2002]), the sky brightness visibility distribution,  $V(u, v)$  mapped on the  $(u, v)$  plane, a 'Fourier plane'.

Here,  $u = \frac{x}{\lambda}$  and  $v = \frac{y}{\lambda}$ . The dirty image,  $I$  is given by:

$$I = R^* \times [C^*(W^* \times V^{*'})] \quad (26)$$

For which, the visibility function is given by:

$$V^* = R(C \times (WV')) \quad (27)$$

where,  $V(u, v)$  is the actual visibility,  $V'(u, v)$  is the measured (noisy) visibility function. Here,  $\times$  and  $*$  denotes the cross product and complex conjugation respectively.  $W(u, v)$  is either the taper,  $(T(u, v))$  or density,  $(D(u, v))$  as the weighting function.  $C(u, v)$  is the gridding convolution, chosen to avoid aliasing.  $R(u, v)$  is the re-sampling function given as,  $\sum_j \sum_k \delta(j - \frac{u}{\Delta u}, k - \frac{v}{\Delta v})$

The receiving system comprises of a number of stages, viz:

- (i) **Phase Lock.** The receiver system starts with a heterodyning stage. The radio frequency (RF) is scaled down to an intermediate frequency (IF). The mixer and local oscillator are used as shown in Figure 13.

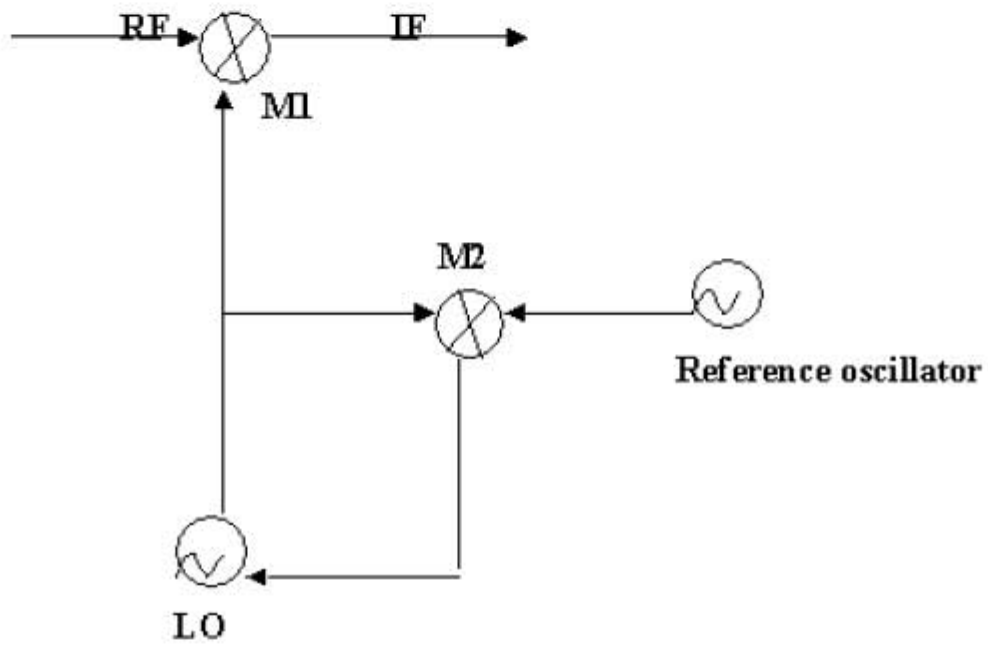


Figure 13: Conversion of RF to IF and phase lock stage. The phase lock system sends an error signal to the LO for correction

The principle of Interferometry involves combining two or more signals from different antennas [Withels, 1975], see Figure 14. One consideration is that, the receivers of the antennas in question operate at the same frequency. This is done using the phase lock system. This uses a reference frequency input that is common to all receivers. The reference frequency is compared with the Local Oscillator (LO) frequency. Any deviation in the phase is communicated to the LO to correct this error.

**(ii) Correlation.** The signal from each receiver assumes the shape of a noisy sinusoidal signal. Part of it is the actual signal from the source but the larger proportion is noise, i.e. the signal to noise ratio is less than one. The source signal can be correlated between the two antennas but the noisy part of the signal cannot since it consists of both the negative and positive components. If we consider time varying voltages,  $V_1(t)$ , and  $V_2(t)$ , their correlation is given by,

$$\gamma = \langle V_1(t)V_2(t) \rangle \quad (28)$$

$$\gamma = \int_{-\infty}^{\infty} V_1(\tau_g)V_2(t + \tau_g)d\tau_g \quad (29)$$

where,

$$V_1(t) = V_1 \cos(2\pi f(t - \tau_g))$$

$$V_2(t) = V_2 \cos(2\pi ft)$$

and  $\tau_g = \vec{B} \cdot \frac{\vec{s}}{c}$  is the geometrical delay of one of the voltages.

Thus,

$$\begin{aligned}
\gamma &= \langle V_1 V_2 \cos(2\pi f(t - \tau_g)) \cos(2\pi ft) \rangle \\
&= V_1 V_2 \langle \cos^2(2\pi ft) \cos(2\pi f\tau_g) + \cos(2\pi ft) \sin(2\pi ft) \sin(2\pi f\tau_g) \rangle \\
&= V_1 V_2 \cos(2\pi f\tau_g)
\end{aligned}$$

This is further simplified to:

$$\gamma = V_1 V_2 \cos\left(2\pi f \frac{B}{c} \sin \Delta\psi\right) \quad (30)$$

$$= V_1 V_2 \cos\left(2\pi \frac{B}{\lambda} \sin \Delta\psi\right) \quad (31)$$

$$= V_1 V_2 \cos\left(2\pi \frac{B'}{\lambda} \Delta\psi\right) \quad (32)$$

$$= V_1 V_2 \cos \Delta\phi \quad (33)$$

The motion of the point source through the interferometer fringe pattern shown in Figures 15 to 18 is due to the slow variation of the cosine term due to variation in  $\tau_g$  as the earth rotates.

The rate at which the source moves through the fringes (fringe rate ( $f_r$ )) is given by Equation (34). The  $f_r$  depends on the geometry of the interferometer.

$$f_r = \frac{\left(\frac{d\omega_s}{dt}\right)}{\frac{1}{B_\lambda \cos HA}} \quad (34)$$

$$= -\Omega_e u \cos \delta \quad (35)$$

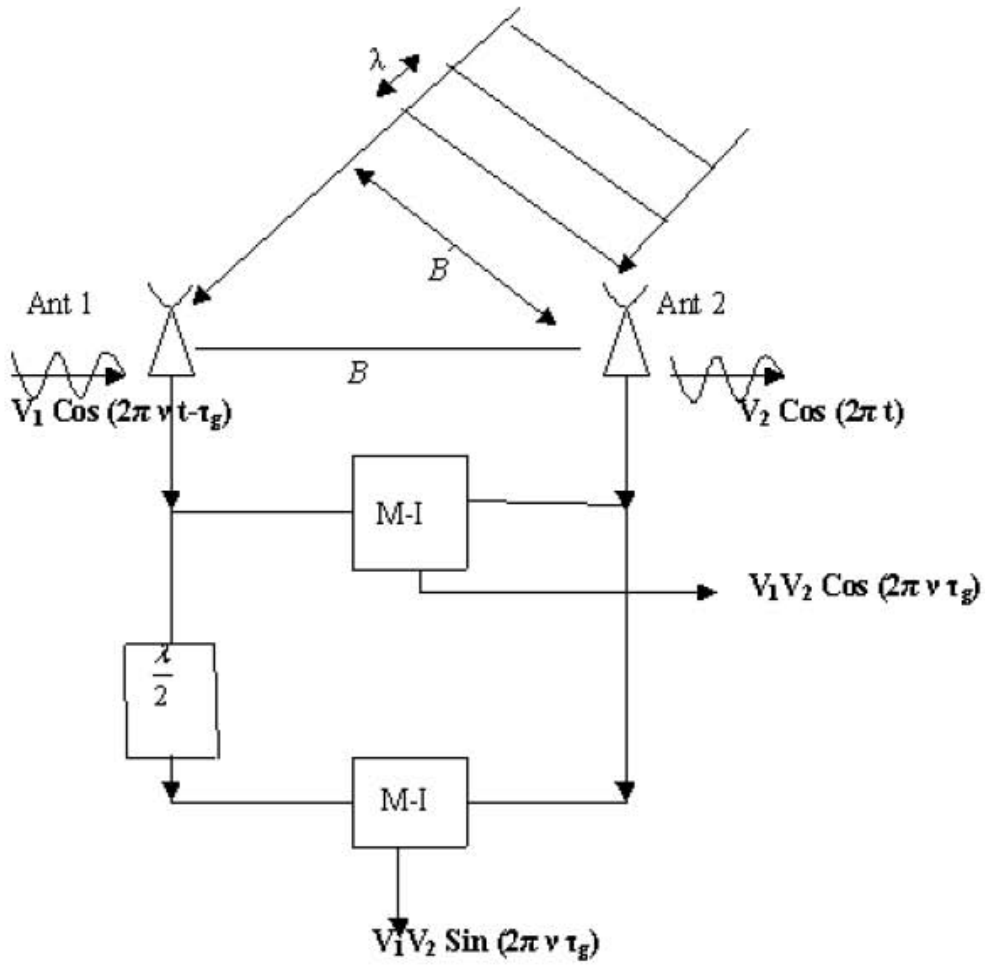


Figure 14: Block diagram for the correlation stage of a radio signal allows the measurement of both the cosine and sine components simultaneously.

where,  $\Omega_e$  is the earth rotation rate [rads/sec],  $\omega_s = \vec{B}_\lambda \cdot \vec{s}_0$  is the spatial frequency and  $\delta$  is the declination. Here,  $\vec{B}_\lambda$  and  $\vec{s}$  are the baseline normalized by a wavelength of radio source signal and unit vectors in the direction of radio wave respectively.  $u = B_\lambda \cos HA$  is the spatial coordinate.

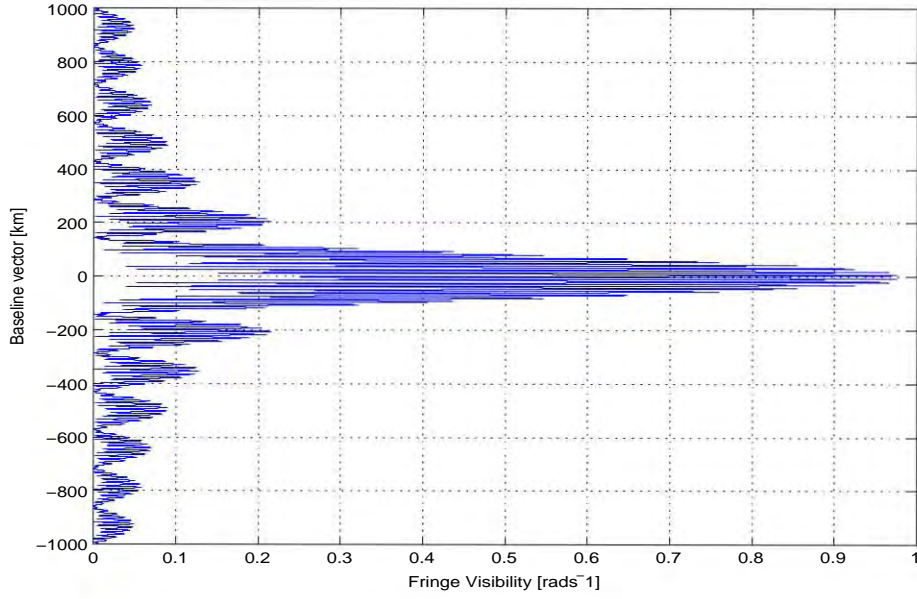


Figure 15: Fringe Visibility dependence on the baseline vector. A double point source is convolved with a single point source to form a double extended source. The visibility reduces with an increase in the baseline vector. The fringe spacing, in radians, ( angular distance between successive maxima ) is given by  $nB_\lambda = \sin \theta_{ab}$ , where  $n = 0, \pm 1, \pm 2, \pm 3, \dots$ . If  $\theta_{ab}$  is small, the fringe spacing is given by  $\Delta\theta_{ab} \approx \frac{1}{B_\lambda}$ . But if  $\theta_{ab}$  is large, the expression for fringe spacing would be  $\Delta\theta_{ab} \approx \frac{1}{B_\lambda \cdot \cos \theta_{ab}}$ .

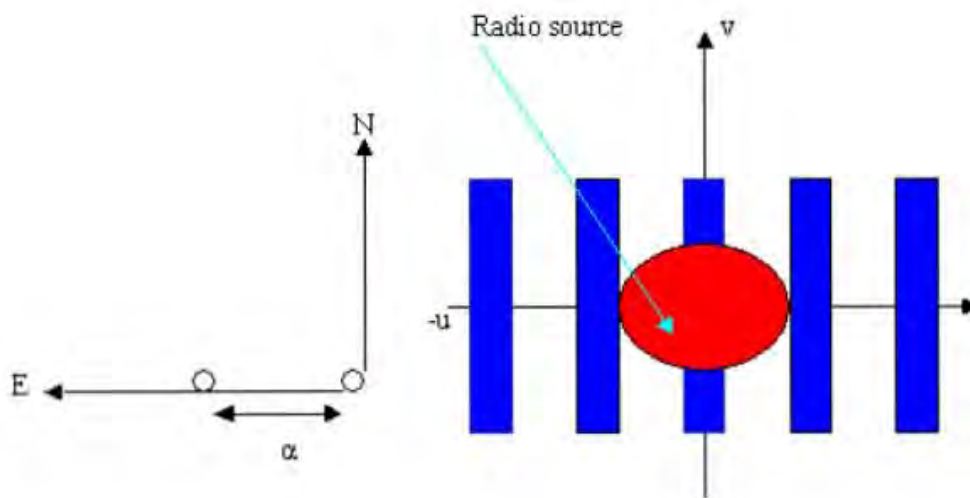


Figure 16: East-West orientation, and the fringes on the  $u$ - $v$  plane, (a spatial plane in the sky perpendicular to the vector  $\vec{s}$ ). The fringe pattern is parallel to the right ascension of the source, (on the  $u$ -axis).

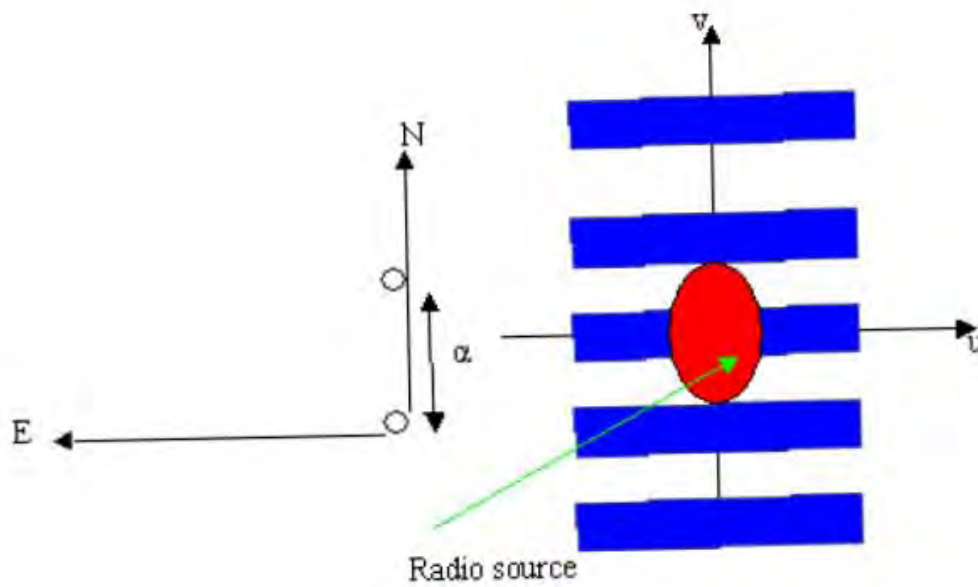


Figure 17: North-South orientation of an interferometer baseline, and the fringes on the  $u$ - $v$  plane. The fringes are on the  $v$ -axis, (parallel to the direction of the declination of the radio source).

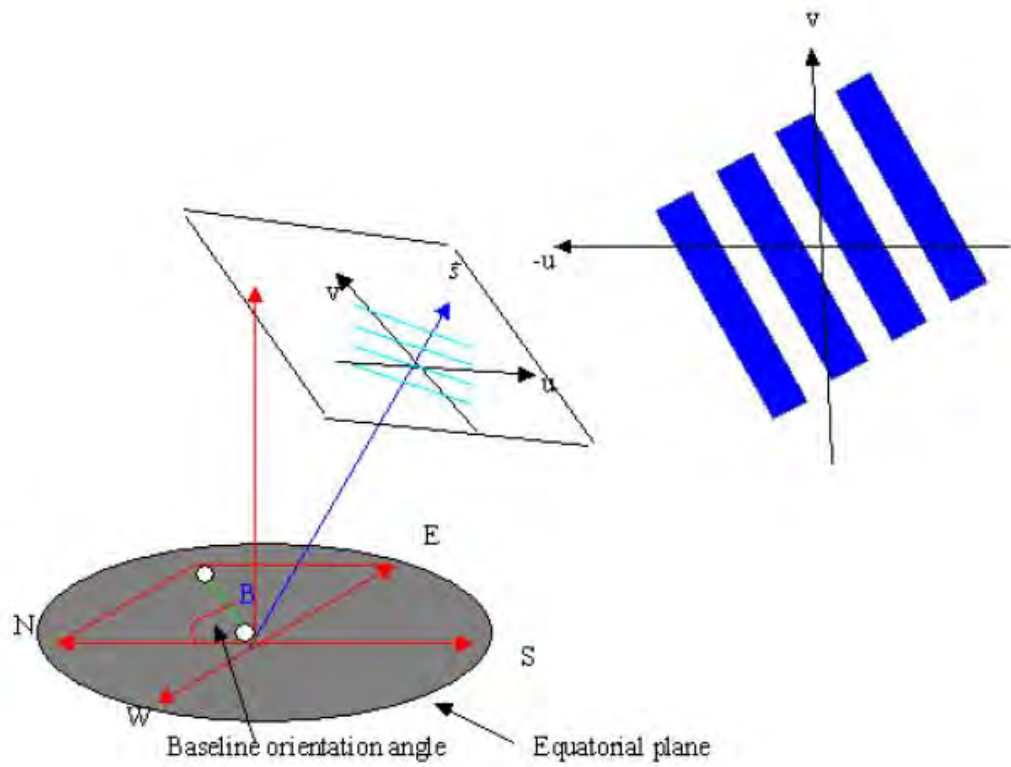


Figure 18: The fringe pattern for which the interferometer baseline orientation is at an arbitrary angle from the North-South geometry.

**(iii) Calibration.** This stage ensures that the measured visibility,  $V'(u, v)$  is as close as possible to the true visibility,  $V(u, v)$ . The true visibility is given by Equation, (36):

$$V(u, v) = \int_{sky} A(l, m)I(l, m)e^{-i2\pi(ul+vm+wn)}dl \cdot dm, \quad (36)$$

Here,  $(l, m)$  are the direction cosines. If phase center is considered, the  $wn$  term representing  $\tau_g f_p$  is zero.  $(u, v)$  is the projected baseline coordinates in wavelengths;  $u = B_{l,\lambda}$  and  $v = B_{m,\lambda}$ .  $V(u, v)$  is the true visibility,  $A(l, m)$  is the normalized primary beam pattern for a single antenna.  $I(l, m)$  is the brightness distribution of the source.

For discrete sampling of the antenna pair,  $(i, j)$  at a time  $t$ , the true visibility when the group delay is compensated for using the fringe fitting method, is expressed as:

$$V_{ij}(t) = \int_{sky} A(l, m)I(l, m)e^{-i2\pi(u_{ij}(t)l+v_{ij}(t)m)}dl \cdot dm, \quad (37)$$

where;  $ul+vm$  is the geometric phase difference,  $\Delta\phi$  due to path length difference between antenna  $i$  and  $j$  with respect to some source location  $(l, m)$  and with respect to phase center.

Using hour angle ,  $h_0$ , and declination  $\delta_0$ , and baseline lengths,  $[B_x B_y B_z]$  the geometric phase difference at the phase center is:

$$\phi_g = 2\pi\tau_g f \quad l=m=0 \quad (38)$$

Since  $\tau_g = \vec{B}_\lambda \cdot \frac{\vec{s}}{c}$ , using the source coordinates, a relationship between the baseline and the source coordinates is;

$$\tau_g \cdot c = \begin{bmatrix} u \\ v \\ w \end{bmatrix} = \lambda \begin{bmatrix} -\sin \delta_0 \cos h_0 & \sin \delta_0 \sin h_0 & \cos \delta_0 \\ \cos \delta_0 \cos h_0 & -\cos \delta_0 \sin(h_0) & \sin \delta_0 \end{bmatrix} \begin{bmatrix} B_x \\ B_y \\ B_z \end{bmatrix} \quad (39)$$

Defining the hour angle in terms of the local sidereal time (*LST*);

$$h_0 = \alpha_0 - LST \quad \text{yielding} \quad dh_0 = d\alpha_0$$

Here,  $\alpha_0$  is the approximated right ascension of the source.

From which we have,

$$\phi_g = 2\pi [B_x \cos \delta_0 \cos h_0 - B_y \cos \delta_0 \sin h_0 + B_z \sin \delta_0] \quad (40)$$

How the errors in source determination as well as those associated with baseline affect the group delay is captured by the differential equation Equation (41).

$$d\phi_g = 2\pi f d\tau_g = \frac{2\pi}{\lambda} \left\{ \begin{array}{l} dB_x \cos \delta_0 \cos h_0 - dB_y \cos \delta_0 \sin h_0 + B_z \sin \delta_0 \\ + d\alpha_0 \cos \delta_0 (B_x \sin h_0) + B_y \cos h_0 \\ + d\delta_0 (-B_x \sin \delta_0 \cos h_0 + B_y \sin \delta_0 \sin h_0 + B_z \cos \delta_0) \end{array} \right\} \quad (41)$$

This equation gives information on the factors affecting the group delay  $\tau(d\phi)$ , i.e. baseline errors ( $\delta B$ ), and the source position errors ( $\Delta\alpha, \Delta\delta$ ).

### 4.3 The Phase Equation

The output of a two element interferometer over an observing frequency bandwidth is a convolution of the instruments' response and the distribution of the source emission [Aller, 2001]. This output exhibits a quasi-sinusoidal time behavior, (also called fringes) which take the form:

$$R(t) = V \cos \phi_T \quad (42)$$

where  $V$  is the amplitude of the fringe pattern and  $\phi_T$  is the total phase delay between the radio signal impinging the two antennas [Fomalont, 1995]. Both are functions of time and direction. The total phase delay consists of a component that depends on the geometric path-length difference of the radio signal travelling to each of the antennas,  $\phi_g$  shown in Equation (43). The total phase delay is also a function of the incoming radio signals. This function co-rotates with the earth.

$$\phi_g = 2\pi f_{av} \left( \frac{\vec{B} \cdot \vec{S}}{c} \right) \equiv 2\pi f_{av} \tau_g \quad (43)$$

where,  $\vec{B}$  is the separation of the phase centers,  $\vec{S}$  is the unit vector in the direction of the center of the source. The vectors  $\vec{B}$  and  $\vec{S}$  are separated by  $\theta_s$ .  $c$  is the speed of light [ $\text{m s}^{-1}$ ],  $f_{av}$  is the average of the signal frequency [Hz]. The other components include the dispersive component  $\phi_d$ , and the visibility phase  $\phi_v$  component which depends on the shape of the source.

In astrometry, the actual fringe phase of a connected element interferom-

eter is derived from the observables. The total phase is given by Equation (44).

$$\phi_T = 2\pi f_{av}(\tau_g + \tau_n) + \phi_d + \phi_v \quad (44)$$

Here,  $\tau_n$  is an additional component that linearly depends on frequency. It is a non-dispersive time delay component, while  $\tau_g$  exhibits dispersiveness. If a reference phase,  $\phi_{ref}$  is expressed by Equation (45),

$$\phi_{ref} = \frac{2\pi \vec{B} \cdot \vec{S}}{\lambda} = \frac{2\pi \vec{B} \sin \theta}{\lambda} \quad (45)$$

then for a source offset, of  $\Delta\theta_s$ , from a reference direction, the observed phase for a point source is given by the phase Equation (46).

$$\phi_{obs} = \frac{2\pi B \sin(\theta_s + \Delta\theta_s)}{\lambda} \approx \phi_{ref} + \frac{2\pi B \Delta\theta_s \cos \theta_s}{\lambda} \quad (46)$$

Equation (46) could be used to compute the position coordinates of the radio source, determine it's structure as well as derive bias errors related to the baseline vector, and the medium through which radio signals propagate. In the next section, I will discuss how a simulated phase observation was used to reconstruct ionospheric phase delay related to pointing errors of an astronomical radio source.

#### 4.4 Simulation of the effects of $TEC$ variability on pointing accuracy of a radio source

I have simulated the effects of ionospheric perturbations on the position of a radio source based on an east-west interferometric array with a point radio source. I have considered a point radio source with coordinates  $85.2^{\circ}$  and  $19.62^{\circ}$  declination and right ascension respectively, and computed the differential phase that would be received from this radio source at an interferometer unit linked by baseline  $B$  using Equation (47).

$$\Delta\phi_{obs} = \frac{2\pi f_{av} B}{c} [\cos D \cos \delta \cos(\lambda' - \alpha) + \sin D \sin \delta] \quad (47)$$

where  $\Delta\phi$  is the received phase difference between two interferometers separated by a baseline vector  $\vec{B}$  [m] and forming an East-West orientation.  $f_{av}$  [Hz] is the mean frequency,  $c$  is the speed of light [ $ms^{-1}$ ], and  $D$  the declination of the baseline vector, taken to be equal to the latitude of the interferometers. For two interferometers on different latitudes,  $B$  is computed from the cartesian coordinate difference of the two geodetic coordinates of the antennas.  $\delta$ , and  $\alpha$  are the declination and right ascension of the radio source.  $\lambda' = A_0 + \Omega_e \cdot t$ , where,  $A_0$  is the right ascension of the unit vector pointing from the phase center to the radio source,  $\Omega_e$  is the angular velocity of the earth, [rad/sec] and  $t$  is the observation time in seconds. The East-West orientation, produces fringes on the u-v plane along the u-axis only, see Figures 16, 17, and 18. This means that, while the rotation of the Earth with respect to the sky helps fill the u-v plane with fringes, the fringe points might

not fill the entire u-v plane even with a long period of observation time. This will in turn lower the quality of the image formed from the Fourier transform of the u-v plane intensity.

Differential phase parameter measurements are simulated, using a 10 minute time epoch with an integration time of 1 second. This integration time is chosen since it corresponds to the time interval during which GPS satellite receivers can provide us with pseudo range observables. I have used the GPS observables to compute the sTEC and thus the phase delay. The pointing error that the ionospheric delay causes while estimating the position of the radio source using the received extra-terrestrial radio signals is determined.

In my simulation, I have estimated errors in radio astronomy source coordinates due to radio signal propagation through the ionosphere. In this simple scenario, I have ignored errors attributed to baseline measurements, radio source structure aliases and clock biases at each interferometer. I also ignored the phase connection, i.e. the  $2\pi n$  ambiguities in  $n$  observations.

Ionospheric phase contributions have been modelled using sTEC computed from the Chapman thin layer approximation and dual GPS pseudo-range observations. Shown in the appendix, is a description of a useful coordinate transformation for computing  $TEC$  using GPS data. Data observed at the two-frequencies (1575.42 and 1227.60 MHz) of the GPS receiver, were used to derive the ionospheric delay of the electromagnetic waves travelling

through the dispersive medium, given in Equations, (48) to (51), presented in [Opperman and Cilliers., 2004] and [Hofmann-Wellenhof, 1997]. The two GPS pseudo-range observables are the code and phase observations. The code pseudo-range  $P_c$  observable is given in terms of the true range,  $\rho$  by the Equation, (48).

$$P_c = \rho + \delta\rho^{ion} + \delta\rho^{trop} + c(\delta t_c^S - \delta t_c^R) + c(b^S + b^R) + \Delta \quad (48)$$

where:

- $\delta\rho^{ion}$ , and  $\delta\rho^{trop}$  are the range errors due to ionospheric and tropospheric delays respectively.
- $\delta t_c^S$ , and  $\delta t_c^R$  are the clock biases of the satellite and receiver clocks respectively. These biases are referenced to the coordinated system of the GPS constellation.
- $b^S$ , and  $b^R$  are the satellite and receiver offset biases, expressed in units of time.
- $\Delta$  is the error due to multi-path interference, satellite phase center offsets, (frequency dependent) as well as the random errors.

The carrier phase pseudo-range observable,  $L$ , is the difference in the phase between the transmitting and receiving oscillators, i.e. the difference between the phase of the receiver oscillator and the signal received plus the number of cycles at the initial start of tracking given by Equation, (49).

$$L = \rho + \delta\rho^{ion} + \delta\rho^{trop} + c \left( \delta t_c^S - \delta t_c^R \right) + \lambda B_g + \Delta \quad (49)$$

where:

- $\lambda$  is corresponding wavelength of the observation
- $B_g$  is the initial phase ambiguity, a frequency specific bias. It is expressed in terms of integer cycles.

The dual frequency receivers provide us with,  $P_{c1}$  and  $P_{c2}$  observables at the two frequencies,  $f_1=1575.42$  and  $f_2=1227.60$  measured in MHz. The observables are used to derive the ionospheric delay, measured in terms of sTEC. If the difference between observables  $P_{c1}$  and  $P_{c2}$  is determined, the identical, frequency independent terms, i.e. the true range term,  $\rho$ , clock offsets, and the tropospheric delay, are eliminated [Opperman and Cilliers., 2004]. Equation (48) becomes:

$$\begin{aligned} \tau_{ion} &= P_{c1} - P_{c2} \\ &= \vartheta \cdot \tau_{ion,1} + c \left( \delta b^S - \delta b^R \right) + \delta\Delta \end{aligned} \quad (50)$$

where:

- $\vartheta = 1 - \frac{f_1^2}{f_2^2} = -0.647$ , is the normalization factor referencing the difference between the  $f_1$  and  $f_2$  ionospheric delays to the  $f_1$ .
- $\tau_{ion,1} = \frac{40.28 \cdot 10^{17}}{f_1^2} TEC$ , is the  $f_1$  related and epoch specific ionospheric delay measured in meters,  $TEC$  is the sTEC.

- $\delta b^S = b^{S,1} - b^{S,2}$  is the differential inter-frequency clock and hardware delay, the differential code bias (DCB)<sup>11</sup> of the satellite, measured in units of time.
- $\delta b^R = b^{R,1} - b^{R,2}$ , is the DCB for the receiver and  $\Delta$  is the difference in the multi-path and random errors.
- $\delta\Delta$  is the differential multi-path and differential random errors.

The phase pseudo-range observables,  $L_1$  and  $L_2$  are expressed in terms of the ionospheric delays at the two frequencies,  $f_1$  and  $f_2$ , given in Equations, (51).

$$\begin{aligned}\tau_{ion}^{phase} &= \delta\rho_{ion,1} - \delta\rho_{ion,2} \\ &= \vartheta\tau_{ion,1} + \delta B + \Delta\end{aligned}\tag{51}$$

where,  $\delta B = \lambda_1 B_1 - \lambda_2 B_2$  is the ambiguity parameter, in units of length. The ambiguity arises from the phase slips and jumps on  $f_1$  and/or  $f_2$ . The cycle slips and jumps occur due to loss of lock in the receivers.

I have neglected second and third terms in Equation (50) and evaluated only sTEC. sTEC computed here is therefore not absolute but is an approximation.

The ionospheric phase delay is injected into the simulated differential phase of the signal from the extra-terrestrial radio source expressed as a linear additive noise:

---

<sup>11</sup>Range values are in the order of  $1 \dots 20$  ns,  $\equiv 2 \dots 60$  TECU [Opperman and Cilliers, 2004]

$$\Delta\phi_{obs} = \Delta\phi_{source} + \Delta\phi_{ion}; \quad (52)$$

where,  $\Delta\phi_{source}$  is the actual clean phase from the astronomical radio source and  $\Delta\phi_{ion}$  is the ionospheric phase delay. Equation, (16) was used to relate the ionospheric phase delay and sTEC.

To determine the position errors,  $[\Delta\delta = \delta - \delta', \Delta\alpha = \alpha - \alpha']$ , that the ionospheric phase perturbation causes, I have used the least square method (LSQ) to compute the parameters,  $\eta_1, \eta_2$ , and  $\eta_3$ , obtained from Equation (53).

$$\frac{c\Delta\phi_{obs}}{2\pi f B \sin D} = \eta_1 + \eta_2 \tan D \cos \lambda + \eta_3 \tan D \sin \lambda \quad (53)$$

$$\eta_1 = \sin \delta' \quad (54)$$

$$\left(\frac{\eta_2}{\eta_3}\right) = \tan \alpha' \quad (55)$$

Where,  $[\delta', \alpha']$  and  $[\delta, \alpha]$  are the estimated and true declination and right ascension of the point radio source.

Irregularities of the ionospheric electron density along a signal path cause rapid and random amplitude and phase fluctuations of a radio signal of the order of 4 seconds, a phenomenon termed scintillation. In the next section, a description of the procedure I used to investigate the occurrence of scintillations will be presented.

## 4.5 Ionospheric Scintillations

Ionospheric scintillations are detected using the dual GPS receiver phase and signal to noise ratio (SNR). I considered the phase scintillation which is

modelled as an additive noise:

$$\phi_r = \phi_0 + \delta\phi \quad (56)$$

where,  $\phi_r$  is the measured phase,  $\phi_0$  is the base phase from the radio source, assuming other bias contributions, and  $\delta\phi$  is the phase scintillation induced by transient ionospheric changes.

For GPS signals, the phase scintillation observable [Wanninger, 1994] is:

$$\delta\phi = \kappa[[\phi_{L2}(t) - \phi_{L1}(t)] - [\phi_{L2}(t-1) - \phi_{L1}(t-1)]] \quad (57)$$

where,  $\phi_{L1}$  and  $\phi_{L2}$  are the GPS phase measurements in L1 and L2 respectively and  $\kappa$  is a constant.

The phase scintillation is a linear process of the electron density irregularity of the ionosphere. It is therefore a gaussian process. To detect the scintillations, the signal is transformed from the time domain to the frequency domain, and a predominant frequency at which these transient fluctuations is detected which is characteristic of the causative mechanism. Different transformation schemes can be used, i.e. wavelet transform(WT)and Fast Fourier transform(FFT). I have used the FFT scheme in my analysis.

I have considered a slowly, sinusoidal variation of the sTEC at timescales larger than the integration time, and Fourier transformed the signal so that the predominant frequency at which the scintillations occur is determined. This frequency is however dependent on the integration time. In the next section, the results of ionospheric *TEC* variation will be presented and discussed, with a typical correction scenario that the proposed SKA might use.

## 5 Results and Discussion

### 5.1 Introduction

The proposed SKA in Southern Africa involves thousands of antennas at different geographic points. This implies that the differential ionospheric delay along path lengths from the radio source to the interferometry pair will be of concern. The Chapman profile fails to show  $TEC$  variability at night time due to anomalous behavior of the sec function for angles greater than  $90^\circ$ . I have used the extended Chapman profile and the Fourier series function to compute predicted slant/vertical total electron content, (sTEC/vTEC) from different sites within the proposed region of the SKA sites. The IRI 2001 was also used to compute vTEC over these sites. This consideration will help show how the baselines affect the differential sTEC. In this way, the geometrical requirements of SKA will include sTEC as an important factor. I have also considered the variation of sTEC with elevation angle.

### 5.2 Predicted sTEC at different locations within the proposed SKA region using the extended Chapman profile

If the SKA array will receive radio signals at a typical frequency band of 1.5–20.0 GHz, then the predicted sTEC computed using the extended Chapman profile and the Fourier series function, could be used to derive the differential ionosphere delay over each proposed SKA antenna at a specific location; (

see Figure 19), pointing towards a radio source.

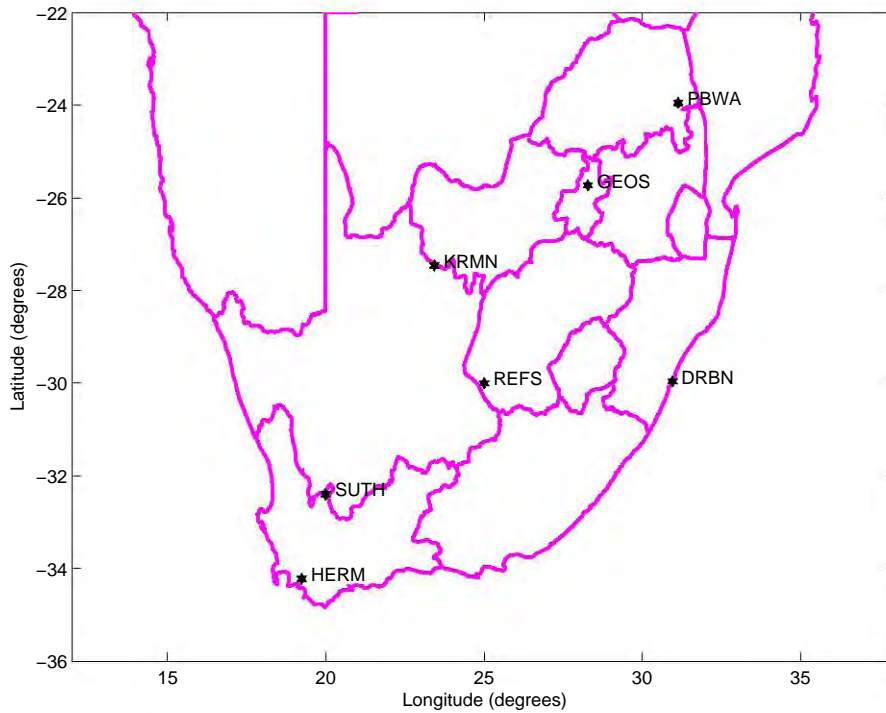


Figure 19: Possible SKA sites in Southern Africa. Most of these stations are positioned alongside GPS receivers.

Figure 20 shows the diurnal  $s\text{TEC}$  variation experienced by the radio signals traversing through the ionosphere for a location at  $[25^{\circ}\text{S}, 20^{\circ}\text{E}]$ . I have used the extended Chapman profile to predict this variation.

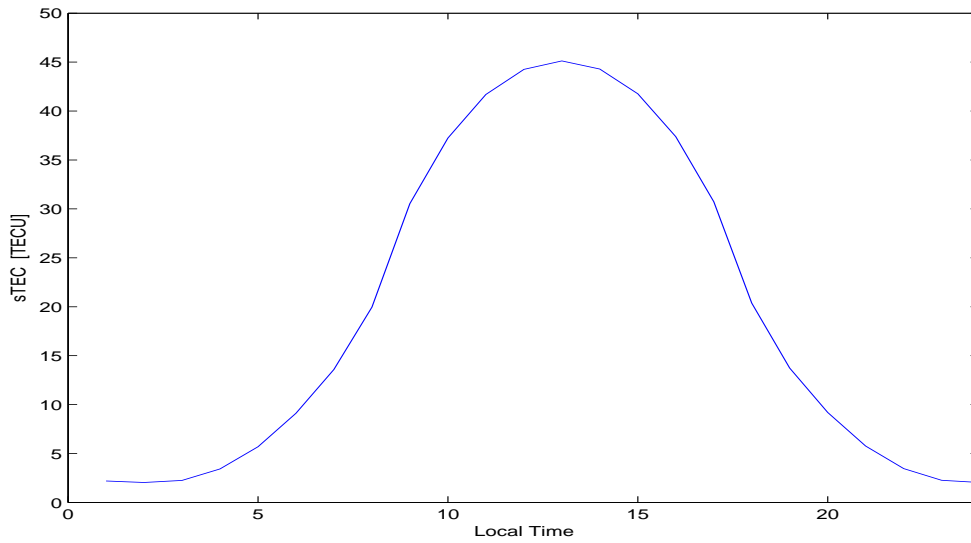


Figure 20: Predicted diurnal sTEC variations caused by the ionosphere, for a location at  $[25^{\circ}\text{ S}, 20^{\circ}\text{ E}]$  in South Africa on 2003-04-11 along azimuth  $35^{\circ}$  and  $25^{\circ}$  elevation.

Figure 20 shows that, by using the extended Chapman profile, a day time sTEC peak value of 45 TECU can be predicted. Night time sTEC values are as low as 2.0 TECU. This implies that a phase delay of  $\approx 255$  radians can be predicted during day time while at night time, the estimated phase delay would be 11 radians at 1.5 GHz. At about 15H00 local time, there are more electrons due to an enhanced ionization from UV and solar x-ray but this fades away at pre-dawn and pre-dusk, due to an enhanced recombination process. Chemical recombination processes involving the neutral atmosphere and other ionized species are favored at sunset and sunrise times since there is reduced UV and X-ray passing through the ionosphere as noted in [Hunsucker and Hargreaves., 2003].

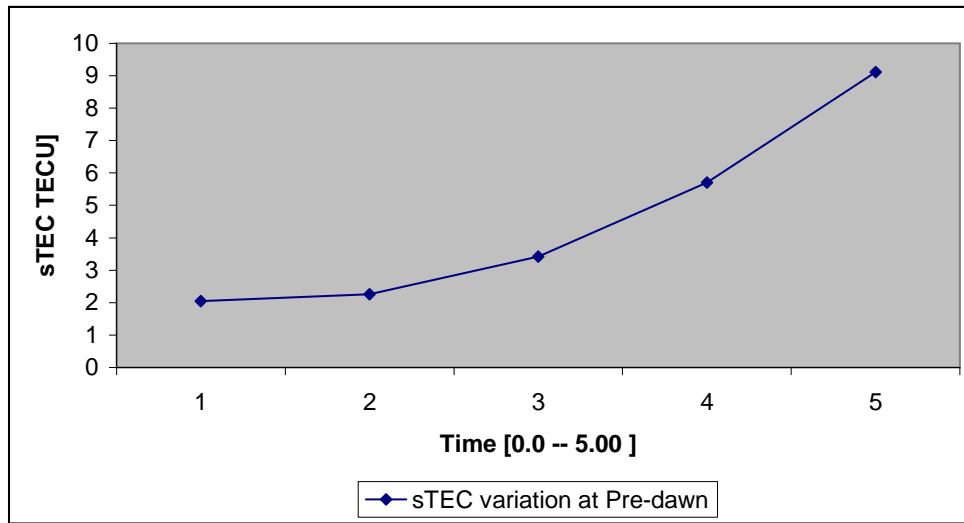


Figure 21: Night time sTEC variation caused by the ionosphere, from a location at [25° S, 20°E] in South Africa on 2003-04-11 between 00H00 to 05H00 hours along azimuth 35° and 25° elevation. These values were derived using the extended Chapman profile.

Night time vTEC variability was investigated using the Fourier series as well as the raised cosine function. Results shown in Figures 21 and 22 are based on the extended Chapman profile.

The Fourier series function, herein referred to as the model function was used to compute vTEC from the seven stations shown in Figure 19. These values were compared to those derived from IRI 2001. Using the reference station (denoted as REFS), longitudinal and latitudinal change of vTEC was estimated. These results are shown in Figures 23. **i-ii**, 24. **i-ii**, 25. **i-ii**. The difference in the standard deviation between IRI 2001 derived *TEC* and *TEC* derived from the Fourier series is 0.2 TECU. The results from all the

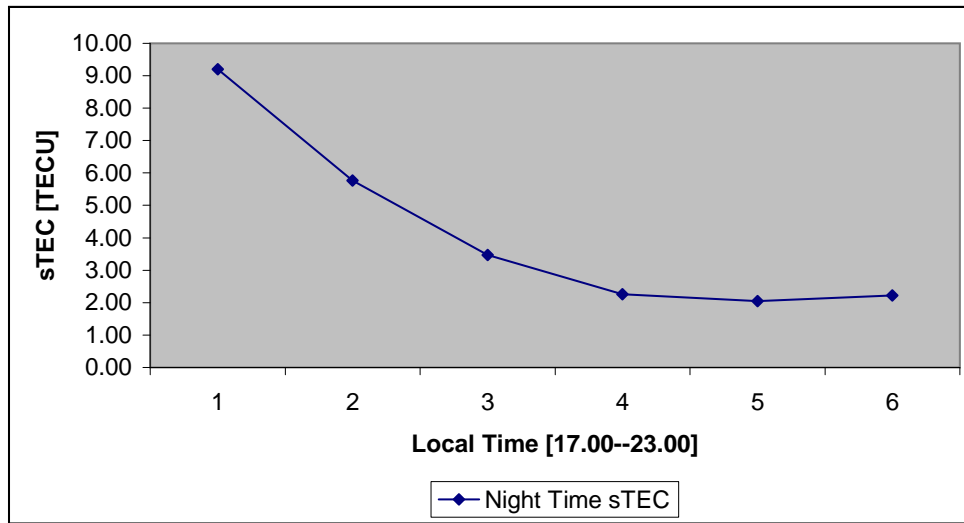
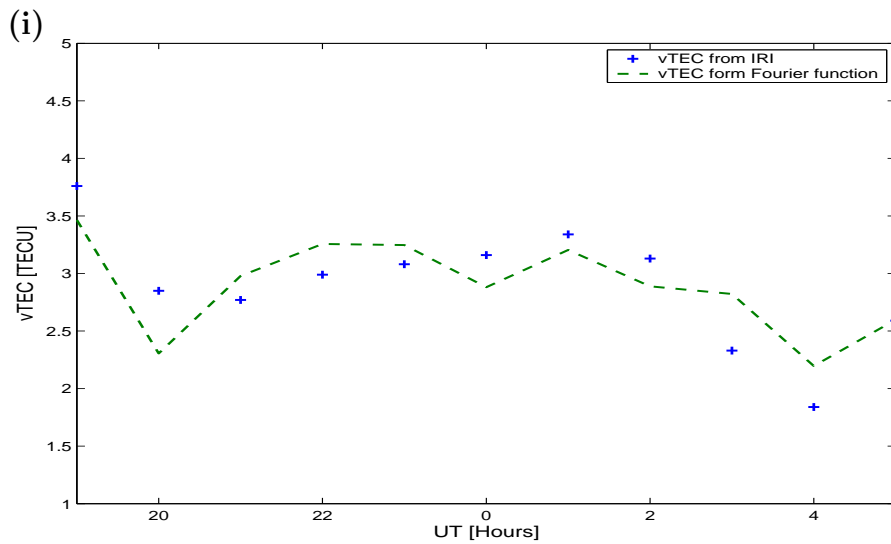
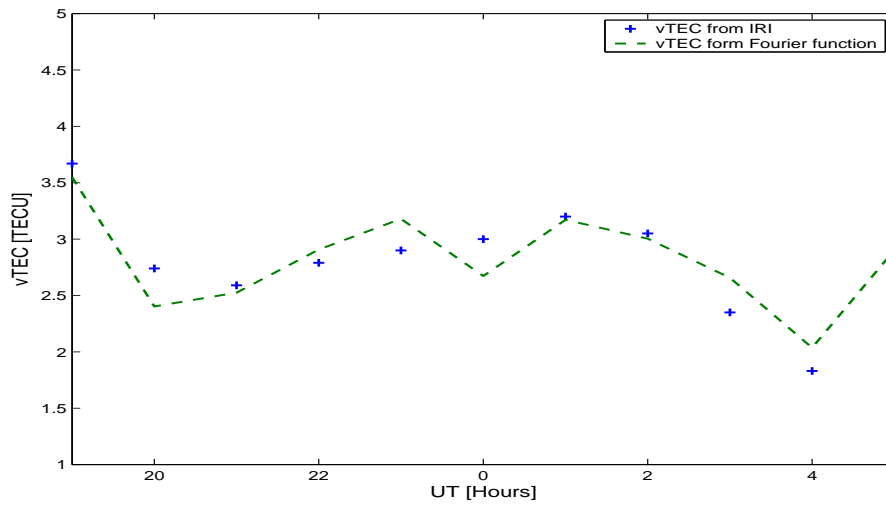


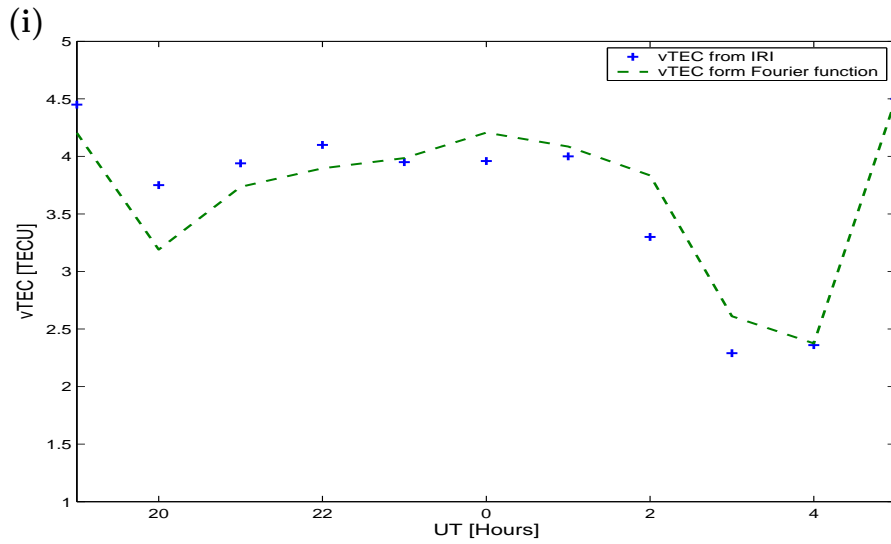
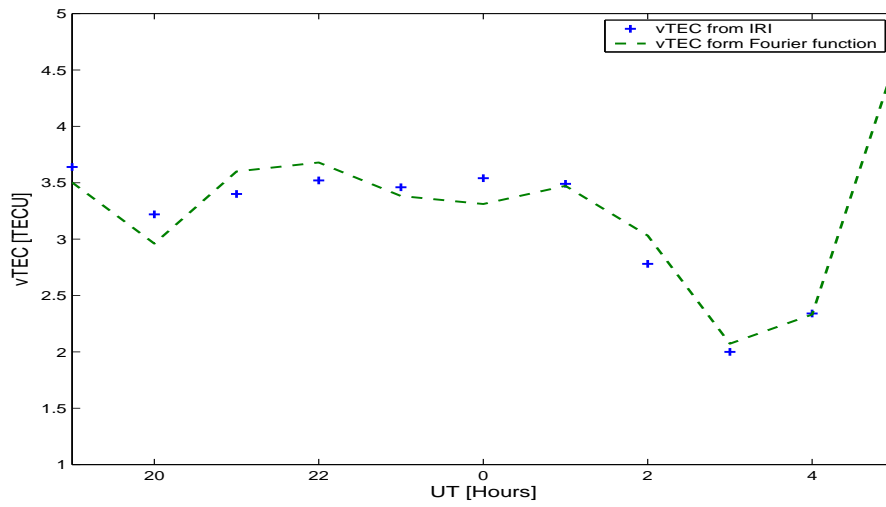
Figure 22: Night time sTEC variation caused by the ionosphere, from a location at [25° S, 20°E] in South Africa on 2003-04-11 between 17H00 to 23H00 hours along azimuth 35° and 25° elevation. These values were derived using the extended Chapman profile.

selected locations show a similar pattern.



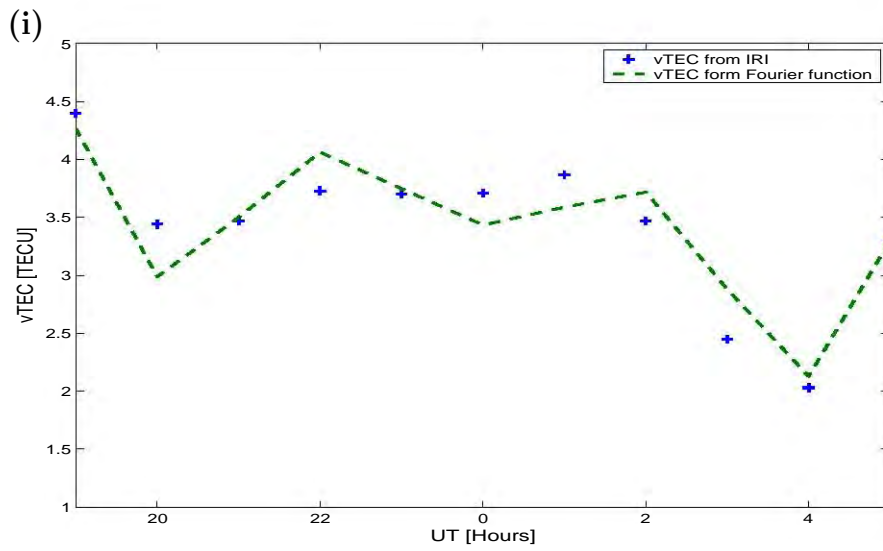
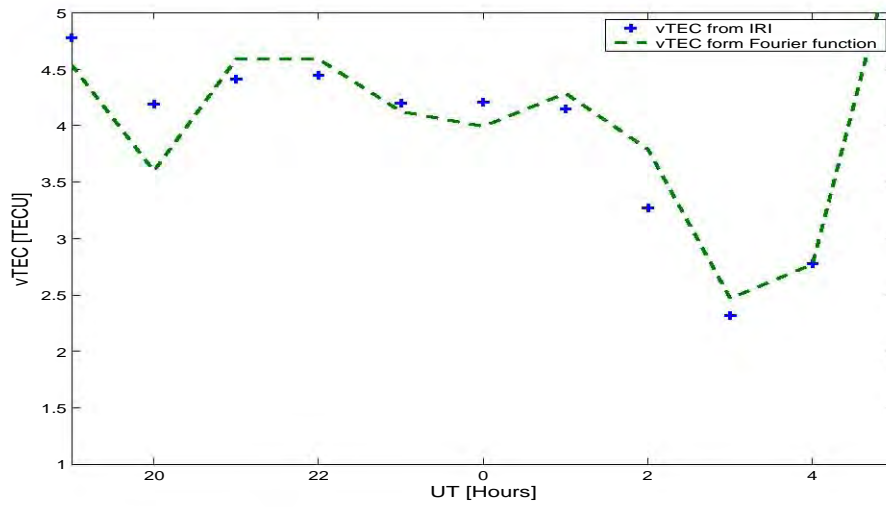
(ii)

Figure 23:  $vTEC$  derived from IRI 2001 data compared with  $TEC$  reconstructed from Fourier series using coefficients obtained from the IRI 2001 data on 2005-05-05 between 18H00 and 06H00 UT at **i-** HERM, **ii-** SUTH .



(ii)

Figure 24:  $vTEC$  derived from IRI 2001 data compared with  $TEC$  reconstructed from Fourier series using coefficients obtained from the IRI 2001 data on 2005-05-05 between 18H00 and 06H00 UT at **i**- DRBN and **ii**- GEOS.



(ii)

Figure 25:  $vTEC$  derived from IRI 2001 data compared with  $TEC$  reconstructed from Fourier series using coefficients obtained from the IRI 2001 data on 2005-05-05 between 18H00 and 06H00 UT at **i-** PBWA, and **ii-** KMAN respectively.

The position of an interferometry pair has an effect on estimated sTEC. If the radio telescopes are placed at different longitudes, the sTEC derived from radio signals received at these positions will vary. The possible longitudinal diurnal sTEC and differential sTEC gradient variation is shown by Figures 26 and 27 on 2003-04-11 for a radio source along azimuth  $35^{\circ}$  and elevation angle  $25^{\circ}$ . The sTEC differential gradient pattern reveals that the variability pattern of *TEC* at two different longitudes is similar but occur at different times. Figure 28 shows that changes in the latitude do not affect the diurnal sTEC as much as the effects induced by longitude changes. The baseline was kept constant as the longitude and latitude positions were varied. For an East-West configuration, sTEC varies linearly with variations in the baseline length. Table 3 shows the absolute peak sTEC derived at latitude  $25^{\circ}$ . Figure 29 shows the variation of differential sTEC for the East-West and North-South configuration. The North-South configuration do not show large diurnal variations in sTEC as compared to the East-West configuration.

The phase delays recorded on the radio telescopes are dependent on the elevation angle of the radio signal ray. Lower elevation angles have higher delays than when compared to the higher elevation angles. This is due to the signal covering a longer path length through the ionosphere at lower elevation angles compared to shorter path lengths at higher elevation angles. Figure 30 shows a peak sTEC variation with elevation angles for a telescope at  $[30^{\circ} \text{ S}, 25^{\circ} \text{ E}]$  with an azimuth angle of  $35^{\circ}$  on 2003-04-11. These values were derived from the extended Chapman profile. The dependence of sTEC on elevation angle is important to SKA since this information would be used

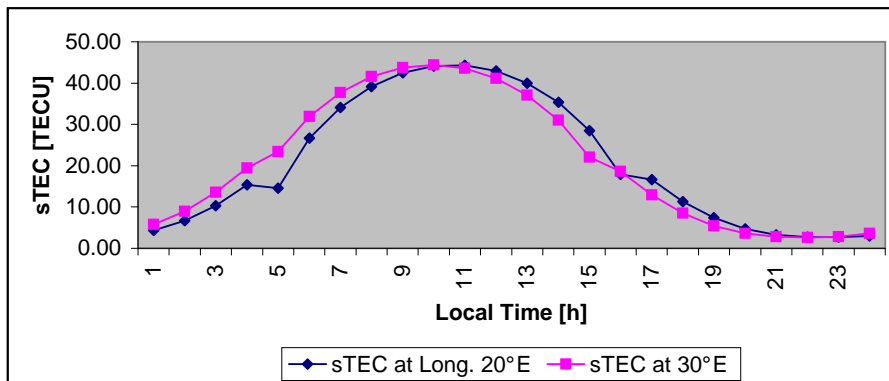


Figure 26: Diurnal sTEC variation at different longitudes from a location:  $[30^{\circ} \text{ S}, 30^{\circ} \text{ E}$  and  $30^{\circ} \text{ S}, 20^{\circ} \text{ E}]$  on 2003-04-11 along azimuth  $35^{\circ}$  and elevation  $25^{\circ}$ .

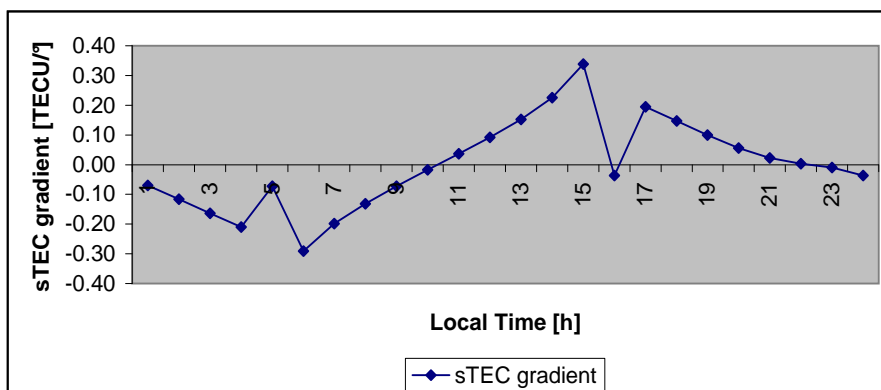


Figure 27: Diurnal changes in differential sTEC longitudinal gradient caused by the ionosphere, from locations:  $[30^{\circ} \text{ S}, 30^{\circ} \text{ E}$  and  $30^{\circ} \text{ S}, 20^{\circ} \text{ E}]$  on 2003-03-11 along azimuth  $35^{\circ}$  and elevation  $25^{\circ}$ . The sTEC gradient remains fairly constant between 07H00 and 14H00 hours.

for determining telescope pointing (elevation cut off angles) angles to a radio

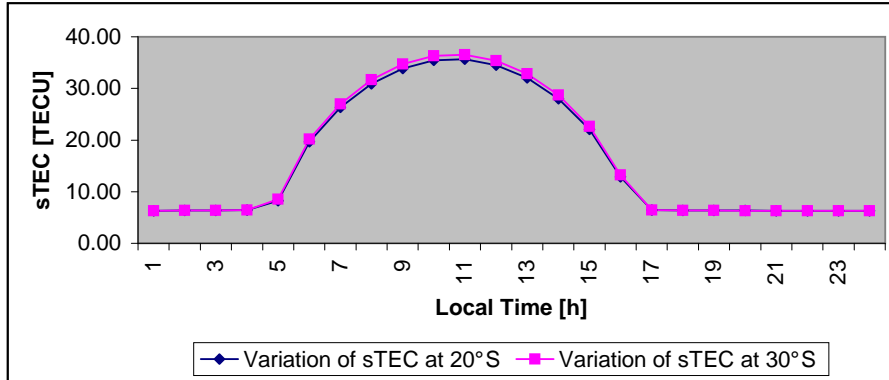


Figure 28: Diurnal sTEC variation at different latitudes from locations;  $[30^{\circ}$  S,  $20^{\circ}$  E and  $20^{\circ}$  S,  $20^{\circ}$  E] on 2003-04-11 along azimuth  $35^{\circ}$  and elevation  $25^{\circ}$ .

Table 3: Predicted peak differential sTEC dependence on baseline length between radio telescopes with an East-West configuration on 2003-04-11 along azimuth  $35^{\circ}$  over latitude  $[25^{\circ}$  S].

Baseline length [km]	Differential sTEC [TECU]
188.14	3.46
376.05	5.07
563.50	8.14
750.27	10.82
936.12	13.14

sky and also rating observations of radio signals. Lowly rated observations would require other means of ionospheric correction or could be discarded.

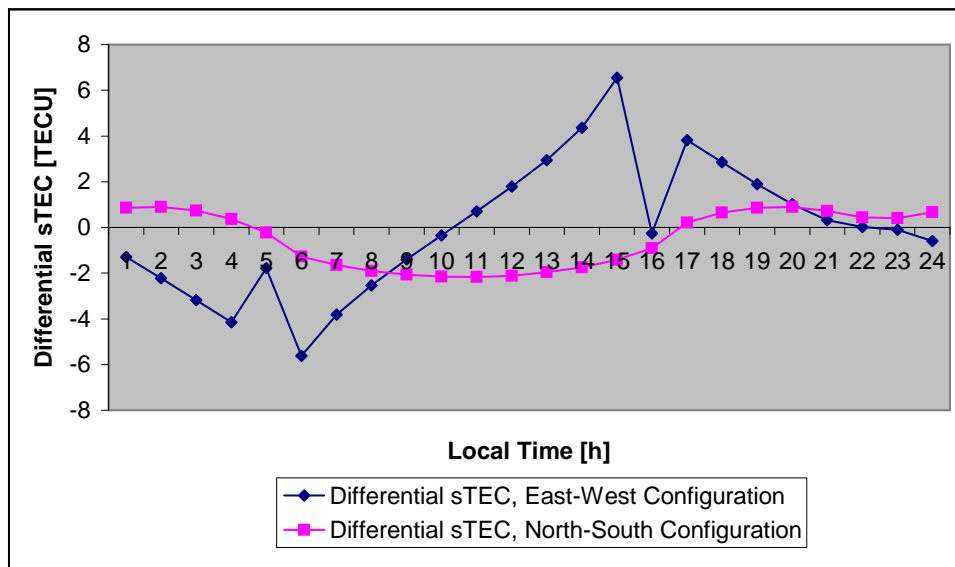


Figure 29: Predicted differential sTEC variation at constant baseline length for radio telescopes with East-West and North-South configuration on 2003-04-11 along azimuth  $35^{\circ}$ . Differential sTEC variation is not highly pronounced in the North-South configuration.

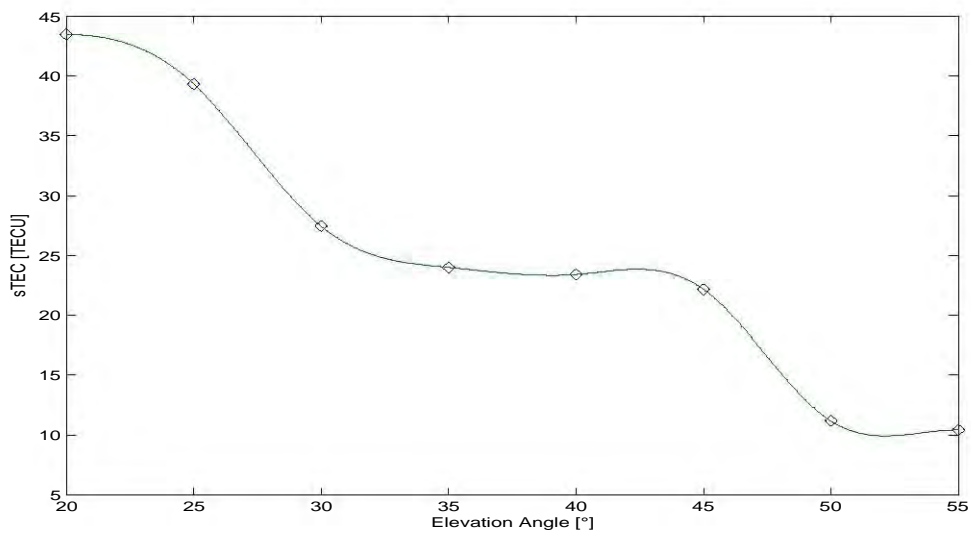


Figure 30: Predicted sTEC variation with elevation angles on 2003-04-11 along azimuth  $35^{\circ}$  from  $[25^{\circ} \text{ S}, 20^{\circ} \text{ E}]$ .

A number of factors must be considered while scheduling radio observations using the SKA array. The geometry of the SKA antenna array, the state of the ionosphere, the nature of the radio sources, the separation angle between the radio and the calibrator sources all prevail on the scheduling program. The ionospheric phase delay (predicted) could be useful for estimating the temporal and spatial changes that the ionosphere causes on the radio signal traversing through it. The effects of the geometry on the receiving antennas can be estimated and factored in during post-correlation data reduction process. Nevertheless, based on the modelled night time values, *TEC* variability in Southern Africa show a consistent pattern with an intermittent spread seen towards dawn. All stations selected exhibited similar trends.

Monitoring of *TEC* gradients over a given region is an important supplement to monitoring scintillations and travelling wave guides. The spatial *TEC* gradients between the reference station and other stations in the network lies between  $\pm 0.5 \frac{TECU}{10}$  longitudinally and latitudinally. This indicates that the ionosphere over the Southern Africa region do not experience abrupt ionospheric changes. This implies that short time ionospheric phenomena like scintillations and short time travelling ionospheric disturbances are unlikely. Again, predicting and monitoring these gradients is possible if the empirical and physical approaches are combined. In the next section, *TEC* variability using GPS data will be examined.

### 5.3 GPS derived *TEC*

Due to the dispersive nature of the ionosphere, dual frequency GPS measurements may provide information concerning the state of the ionosphere by deriving parameters that characterize it such as *TEC* and differential *TEC*. This is done by computing differential code and carrier phase measurements. To a first approximation, the differential phase delay obtained from the difference between L1 and L2 phases is proportional to the total electron content along a ray path between a GPS transmitter and receiver. Through a linear combination of the L1 and L2 observations, the ionospheric delay can also be eliminated. Of concern to SKA is the advantage that from the dual-frequency measurements, we can remotely sense the ionosphere.

Tables 4 to 7 show tabulated results of sTEC and Pseudo Vertical *TEC* (pVTEC) for the satellites, identified by their SV numbers at different elevation angles from the Hermanus (HER) dual GPS receiver station for the different time epochs; 00H00, 06H00, 12H00, 20H00 UTC as derived from the GPS data recorded on 2003-04-11.

SV no.	Elev, [Degrees]	sTEC, [TECU]	pVTEC, [TECU]
7	28.87	47.63	32.71
5	31.63	59.99	43.50
4	48.17	47.32	42.91
10	50.92	59.91	55.50
24	61.59	51.99	50.78

Table 4: *TEC* (in TECU) values on 2003-04-11 at 00H00.

SV no.	Elev, [Degrees]	sTEC, [TECU]	pVTEC, [TECU]
26	30.10	64.37	45.37
15	59.40	57.90	56.13
23	57.40	57.84	55.61
18	57.48	56.09	53.94
17	63.97	44.67	43.92
9	65.37	55.70	54.94
21	65.56	37.27	36.78

Table 5: *TEC* (in TECU) values on 2003-04-11 at 06H00.

SV no.	Elev, [Degrees]	sTEC, [TECU]	pVTEC, [TECU]
2	21.54	110.09	89.68
14	24.82	114.29	71.39
6	26.52	–	–
20	32.43	110.84	81.74
16	67.97	80.49	79.77
25	56.99	86.44	82.95

Table 6: *TEC* (in TECU) values on 2003-04-11 at 12H00. P1 value for satellite SV.6 was not present.

SV no.	Elev, [Degrees]	sTEC, [TECU]	pVTEC, [TECU]
22	28.74	41.68	23.17
31	34.20	46.04	28.57
28	37.76	41.68	33.56
27	57.39	52.56	45.17
8	64.35	50.05	45.64
11	66.99	33.86	31.45

Table 7: *TEC* (in TECU) values on 2003-04-11 at 18H00.

Tables 4 to 7 show that the average sTEC and pVTEC values vary with the time of the day. At 00H00 and 18H00 UTC, pVTEC are at a minimum compared to pVTEC derived at 12H00. This is to be attributed to the difference in the path lengths through which the radio signal transmitted from the satellite propagates. sTEC is derived from slant range that is longer compared to the near vertical path length from which pVTEC is derived, see Equation (21). Figure 31 shows the transient variations of slant *TEC* for a short time interval of 10 minutes at midday. The sTEC is computed using GPS data sampled at one second intervals at the Hermanus GPS station.

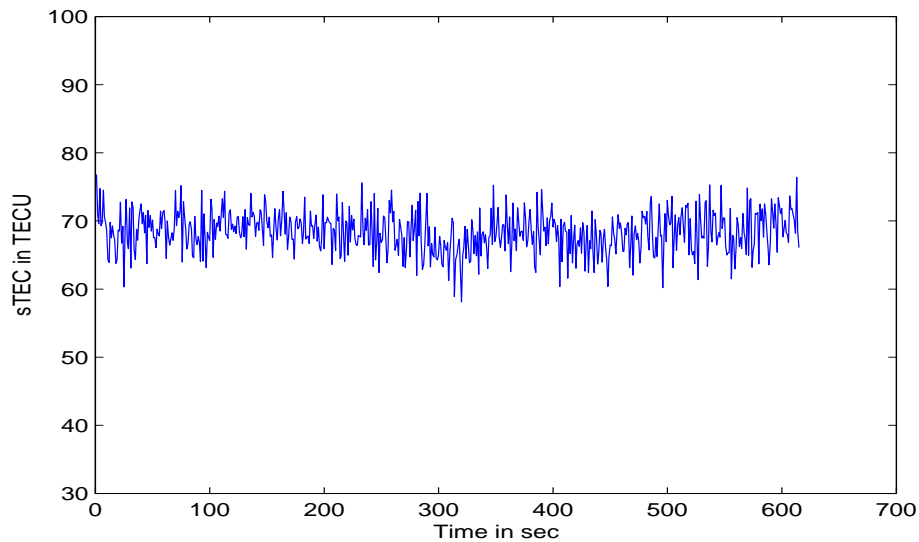


Figure 31: Snapshot [a 10 minute window] of the variation of sTEC derived from GPS observation data recorded at Hermanus dual frequency receiver station on 2003-04-11.

I used GPS data to investigate scintillations by transforming the additive sum of the phase delays due to ionospheric sTEC and the simulated phase

from the radio source to the frequency domain using FFT. Results from the FFT signal did not have any significant frequency. This implies that the scintillations were absent in the data that I considered, see Figure 32. Generally, scintillations have been observed and are limited to mid-latitudes and high latitudes as opposed to low latitudes. To verify that the Matlab code I used would detect the scintillations if they were present, I used a base sTEC and computed the corresponding phase delay. This was then mapped to a sinusoidal function at a frequency, defined by the observation time interval and was then Fourier transformed. The results captured the predominant frequency, see Figure 33.

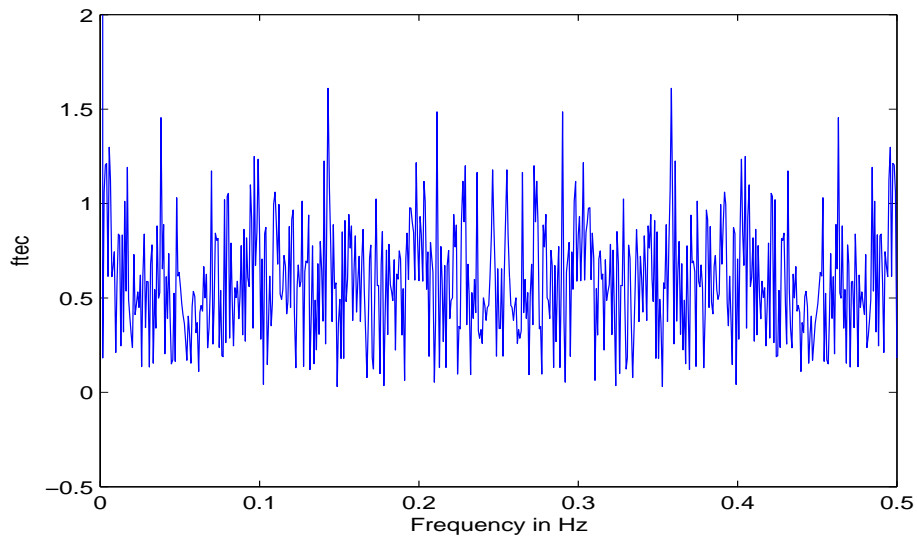


Figure 32: Fourier transform of sTEC derived from GPS data recorded at Hermanus dual frequency receiver station on 2003-04-11. The ftec is the FT of sTEC. There is no noticeable dominant frequency, indicating that the scintillations are absent.

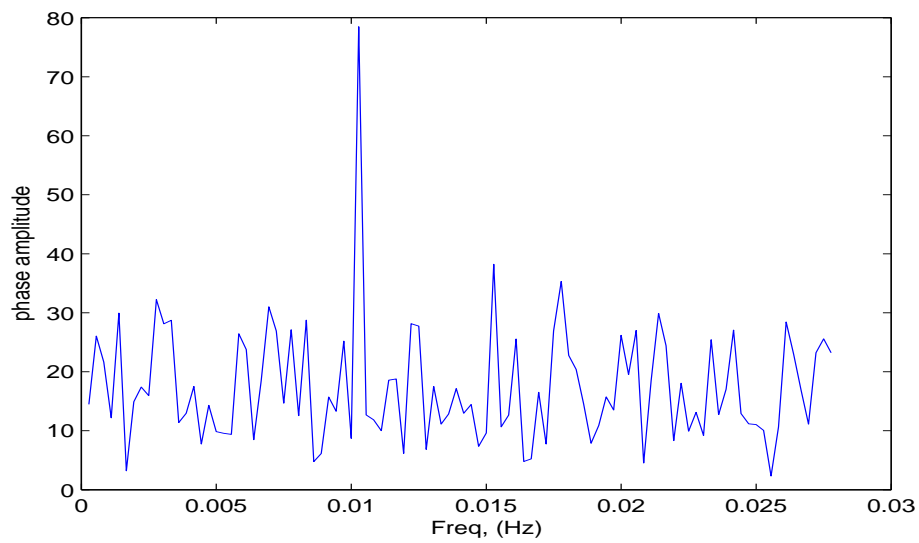


Figure 33: Fourier transform of sinusoidal sTEC by a dominant Frequency of 0.01 Hz. This is an indication that the scintillations characterized by 0.01 Hz could be detected if they were present in the 10 minute snapshot GPS data recorded between 10H00 and 10H10 for a satellite at an elevation of  $32.34^{\circ}$ .

## 5.4 Pointing errors due to phase delay

I have used predicted and observed sTEC to estimate the error in declination and right ascension of a radio source at  $[\alpha = 19.62^0, \delta = 85.20^0]$ . I have simulated differential phase delays of the radio signal propagating through the ionosphere and received the signal at two radio signals for a time period of 10 minutes. The differential phase delay is related to the source coordinates and position errors computed from Equations (47) and (53). Table 8 shows the pointing errors arising from ionospheric delay of a radio signal passing through the ionosphere as predicted using the modified Chapman profile at different positions, (thus baselines) along the same line of latitude ( $30^0$  S).

Table 8: Predicted radio source pointing errors induced by the ionosphere computed by the extended Chapman profile. The pointing errors are in order of milliarcseconds *mas* as reported in literature [P ere-Torres et al, 2000].

Longitude difference, [ $^0$ ]	3.0	5.0	7.0	9.0
Baseline, B [km]	329.92	549.75	769.41	988.85
$\Delta\delta$ , [ <i>mas</i> ]	20.92	10.28	5.85	4.08
$\Delta\alpha$ , [ <i>mas</i> ]	2.86	1.72	0.99	0.57

I also used a typical mid-day sTEC computed from GPS data and computed the radio source position errors due to the signal propagation through the ionosphere at different baseline lengths. From the results, pointing errors of the order of *mas* can be estimated from the measured sTEC, see Table 9. Measured and predicted ionospheric sTEC can therefore be useful in cor-

recting the pointing errors that arise from phase delays due to the ionosphere.

Table 9: GPS derived sTEC effect on radio source pointing errors. The pointing errors are higher in order of magnitude to those predicted by the extended Chapman model.

Baseline, B [km]	329.92	556.41	778.74	1000.80
$\Delta\delta$ , [ <i>mas</i> ]	25.47	12.48	6.90	4.59
$\Delta\alpha$ , [ <i>mas</i> ]	7.22	4.34	2.20	1.67

## 6 Conclusion

The SKA frequency spectrum is sensitive to the conditions of the mid-latitude ionosphere. The parameters that characterize the state of the ionosphere;  $TEC$ , differential  $TEC$  as well as slab thickness can be derived from observed (GPS) and predicted (Chapman) data. The ionospheric spatial and temporal differential  $TEC$  variability induces phase delays and transient fluctuations on the radio signal propagating through it.

Simulated results for the South African SKA array show that, the measured and predicted differential  $TEC$  and  $TEC$  variability cause phase delays of the order of 10-200 radians. These phase delays translate to an order of milliarcseconds in pointing offsets of a radio source position. These pointing errors can be corrected for if differential  $TEC$  is known in near real time. Data from which differential  $TEC$  and  $TEC$  variability could be reconstructed from is available [at one second intervals] at the GPS ground receivers in South Africa. This can be supplemented using the modified Chapman profile which includes night time conditions. The extended Chapman model presented here is not conclusive. Future refinements are required to include initial input parameters like the electron density, the scale height and coefficients of the polynomial function so as to represent the physical conditions of the ionosphere. In this way, a good model describing the diurnal ionospheric conditions through the radio signals received by the proposed SKA antennas could be derived.

The occurrence of scintillations caused by the ionosphere can also be monitored using the observed GPS data. A 10 minute snapshot of the data

(10H00 to 10H10) recorded by the Hermanus dual GPS receiver on 2003-04-11, was processed and results showed no noticeable scintillations. The time used here is not representative and monitoring over longer time scales (Hours and days) is needed for comprehensive prediction of scintillations.

Simulated results show that the SKA antenna geometry, affects the estimation of differential *TEC* and *TEC* variability. This translates to different phase delays for different antenna pairs, if the antenna dependent effects on the signals are ignored for simplicity. This implies that, antenna dependent ionospheric correction schemes would be needed. The flow chart shown in Figure 34 shows ionospheric correction stages that would be appropriate to SKA.

In conclusion, the current GPS receiver network can provide data from which ionospheric phase delays could be corrected for in near real time. Further investigation on the use of predicted and observed data for temporal and spatial modelling of the ionosphere is necessary.

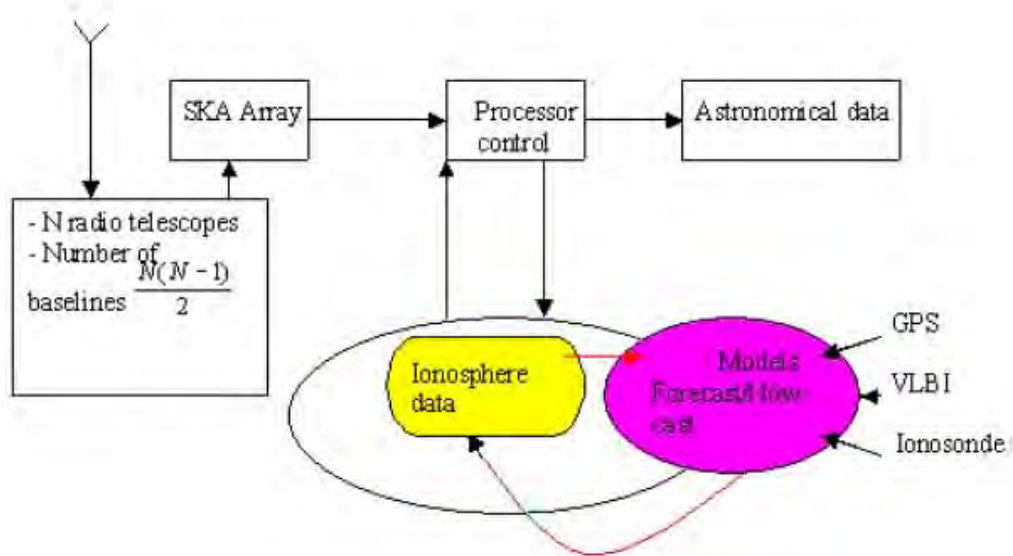


Figure 34: Typical SKA ionosphere correction process.

## 7 Appendix : Transformations

A number of Transformations are required to place different points in the same coordinate system. To correctly describe GPS satellite positions, we need to know the position of the earth receiver as well as the position of the satellite in orbit. The position of the receiver is described by the geographic or geodetic coordinate system. These coordinates are transformed to Earth-centered Earth-fixed (ECEF) coordinates. The satellite position is described by either the satellite orbit and orbit orientation in space-plane coordinate system, right ascension-declination, and the azimuth, elevation and range coordinate system.

A few coordinate systems will be described herein. Details of other transformations are presented on a separate article and will be available on request. The symbols and abbreviations used here are local; they denote parameters discussed in the appendix only and should not be confused if ever used earlier.

### 7.1 ECEF, Geocentric and Geodetic coordinate systems

A geodetic position of the Earth station is described on an ellipsoidal surface by geodetic latitude and longitude,  $[-\frac{\pi}{2} \leq \psi_e \leq \frac{\pi}{2}]$  and  $[-\pi \leq \lambda_e \leq \pi]$  respectively, while the six Keplerian elements are used to describe the celestial position of the satellite.

The simplest case of a coordinate system is ECEF coordinate system.

Here, the three orthogonal axes define the coordinate system, see Figure 35. The Z-axis coincides with earth's rotation axis and the X-Y plane coincides with the equatorial plane. This is sometimes referred to as the local cartesian coordinate set. It assumes that the center of the earth is the origin of the coordinate system. The geocentric coordinate system is quite similar to the above but differ only in the parameter specification. Instead of specifying the set XYZ as in ECEF system, the geocentric coordinate system uses the longitude, the latitude and height above an ellipsoid.

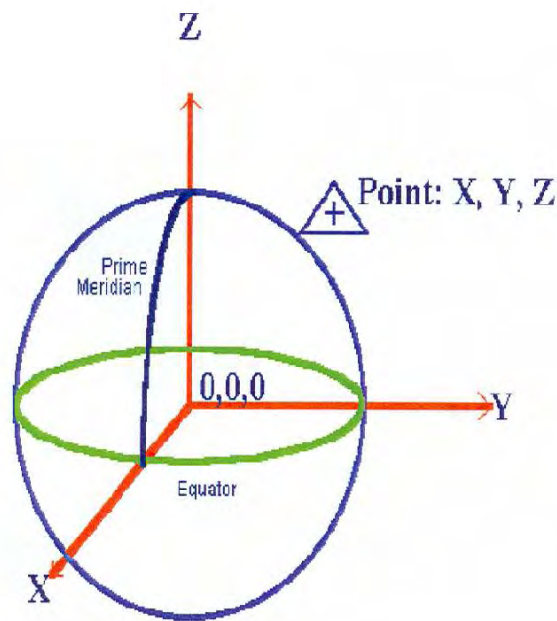


Figure 35: Cartesian coordinates

The coordinates of an observer in the World Geodetic System, 1984 (*WGS84*) given as longitude, latitude and height (LLA) can be transformed to ECEF (XYZ) coordinates using the following equations:

$$X = (N_c + h_c) \cos(\psi_c) \cos(\lambda_c) \quad (58)$$

$$Y = (N_c + h_c) \cos(\psi_c) \sin(\lambda_c) \quad (59)$$

$$Z = \left( (1 - e_c^2) N_c + h_c \right) \sin(\psi_c) \quad (60)$$

where,  $\phi_c$  is the latitude in degrees,  $\lambda_c$  is the longitude in degrees,  $h$  is the height above the *WGS84* ellipsoid in metres,  $a$  and  $b$  is the semi-major and semi-minor axis,  $e_c$  is the eccentricity,  $N_c$  is the radius of curvature, in metres expressed as;

$$N_c = \frac{a}{\sqrt{1 - e_c^2 \sin^2 \psi_c}} \quad (61)$$

The above equations use the *WGS84* parameters given in Table 10.

Name	Notation	Value	Units
Semi-major axis	a	6378137.00	m
Semi-minor	b	$a(1 - f)$	m
First eccentricity	$e_c$	$\sqrt{\frac{a^2 - b^2}{a^2}}$	—
Flattening	$f$	$\frac{1}{298.257223563}$	—
Ecc.Squared	$e_c^2$	$2f - f^2$	—

Table 10: WGS84 Ellipsoid Parameters

Table 11 shows the input (LLA) and the resulting output from the trans-

formation. The percentage deviation from the original coordinates is also shown.

Table 11: Geocentric conversion to ECEF coordinates

-	<b>Input-LLA</b>	<b>Output-LLA</b>	<b>Perc.Error(LLA)</b>
Latitude [°]	-20.0	-20.0	0.00
Longitude [°]	30.0	-30.0	0.00
Height [m]	0.0	-29.4	0.03
Latitude [°]	40.0	40.0	0.00
Longitude [°]	60.0	60.0	0.00
Height [m]	60.0	60.0	0.00

Similarly, Table 12 shows the results of the transformation; XYZ transformed to LLA and then back to XYZ values, .

Table 12: ECEF conversion to Geocentric coordinates

-	<b>Input-XYZ [km]</b>	<b>Output-LLA [km]</b>	<b>Perc.Error(XYZ)</b>
X	4500.00	4500.00	$5.1 \cdot 10^{-4}$
Y	1850.00	1850.00	$1.1 \cdot 10^{-5}$
Z	4110.00	4109.99	$6.3 \cdot 10^{-5}$
X	4796.68	4796.68	$3.3 \cdot 10^{-5}$
Y	2930.34	2930.34	$1.4 \cdot 10^{-5}$
Z	-3005.45	-3005.34	$3.6 \cdot 10^{-3}$

For the inverse transformation, the following closed equations could be used:

$$\lambda_c = \tan^{-1} \frac{Y}{X} \quad (62)$$

$$\psi_c = \tan^{-1} \left( \frac{Z + e_{c1}^2 b \sin^3 \theta}{p - e_c^2 a \cos^3 \theta_c} \right) \quad (63)$$

$$h_c = \frac{p}{\cos \psi_c} - N_c \quad (64)$$

$$e_{c1} = \sqrt{\frac{a^2 - b^2}{b^2}} \quad (65)$$

where  $p$  and  $\theta_c$  are expressed as:

$$p = \sqrt{X^2 + Y^2}$$

$$\theta_c = \tan^{-1} \left( \frac{Za}{pb} \right)$$

The results from these transformations show that transforming from LLA to ECEF and back to LLA and vice versa yields errors of transformation in the order of mm.

In the transformation from geocentric to geodetic coordinates, the geocentric (LLA) coordinates are converted to cartesian coordinates. From the cartesian coordinates, they are transformed to geodetic coordinates using Vincenty formulae [Vincenty, 1980].

$$\tan \psi_{c1} = \left( \frac{a_1}{b_1} \right)^2 \left( \frac{Z}{P} \right) \left[ 1 + \frac{e_c^4 h_{c1} a (Z^2 - P^2)}{4a_1} \right] \quad (66)$$

$$T = \frac{(P - h_{c1} \cos \psi_{c1})^2}{a^2} \quad (67)$$

$$U = \frac{(Z - h_{c1} \sin \psi_{c1})^2}{b^2} \quad (68)$$

$$h = h_1 + \frac{T + U - 1}{2 \left( \frac{T}{a} + \frac{U}{b} \right)} \quad (69)$$

$$\psi_c = \tan^{-1} \left[ \left( \frac{a}{b} \right)^2 \frac{Z - e_c^2 h \sin \phi_{c1}}{P} \right] \quad (70)$$

$$\lambda_c = \tan^{-1} \left( \frac{Y}{X} \right) \quad (71)$$

$$(72)$$

Where:

$$b = a(1 - f)$$

$$P^2 = X^2 + Y^2$$

$$r^2 = P^2 + Z^2$$

$$h_{c1} = r - a + \frac{(a - b) Z^2}{r^2}$$

$$a_1 = a + h_{c1}$$

$$b_1 = b + h_{c1}$$

Dana's formulae [Dana, 1999] are used for inverse transformation. Here, the geodetic coordinates are converted first to cartesian coordinates. Using this cartesian coordinates, the geocentric coordinates are computed.

$$C = \cos^2 \psi_c + \left( (1 - f) \sin^2 \right)^{-0.5} \quad (73)$$

$$S = C(1 - f)^2 \quad (74)$$

$$P = \sqrt{X^2 + Y^2} \quad (75)$$

$$e_{c1} = \frac{a^2 - b^2}{b^2} \quad (76)$$

$$\theta_c = \tan^{-1} \frac{Za}{pb} \psi_1 = \tan^{-1} \left( \frac{(Z + e_{c1}^2 b \sin^3 \theta_c)}{(P - e_c^2 a \cos^3 \theta_c)} \right) \quad (77)$$

$$N_c = \frac{a}{\sqrt{(1 - e_c^2 \sin^2 \theta_c)}} \quad (78)$$

$$h_c = \left( \frac{p}{\cos \psi_{c1}} \right) - N_c \quad (79)$$

$$\lambda_c = \arctan 2(Y, X) \quad (80)$$

Figure 36 shows the relation between geodetic and geocentric coordinates.

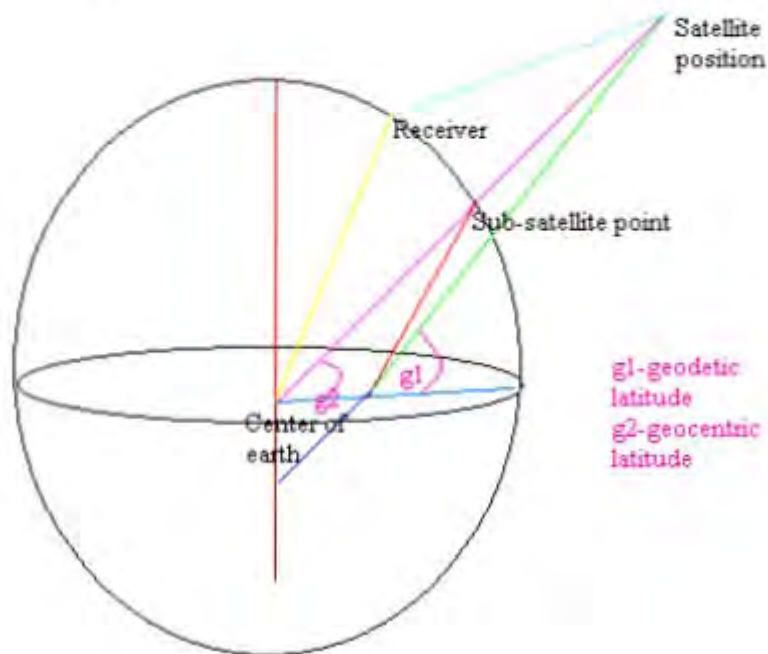


Figure 36: Geocentric and Geodetic coordinate system

Table 13 shows the input and output values during the conversion from geocentric coordinates to geodetic and back to geocentric coordinates.

## 7.2 Satellite Orbit-coordinate systems.

The path of the satellite orbiting round the Earth takes the form of an ellipse. The parameters described below are used to specify the shape of the orbit, and position of the satellite in orbit.

Table 13: Conversion from Geocentric to Geodetic and back to Geocentric coordinates.

<b>Input</b>	<b>Output</b>	Percentage deviation
Lat=60.00 <sup>0</sup>	60.023 <sup>0</sup>	0.04
Lon=40.00 <sup>0</sup>	40.00 <sup>0</sup>	0.00
h=0.00 m	0.0002 m	0.02
Lat=-30.00 <sup>0</sup>	-30.17 <sup>0</sup>	0.57
Lon=-20.00 <sup>0</sup>	-20.00 <sup>0</sup>	0.00
h=1250.00m	1198.15 m	4.15

### 7.2.1 Satellite Orbit-plane

**Period of Revolution.** This is time taken by the satellite to revolve around the Earth. It is given by the formula.

$$P = \frac{2\pi}{\kappa_s \sqrt{\mu_s}} \cdot a_s^{\frac{3}{2}} \quad (81)$$

Where  $P$  [seconds], is period of revolution,  $\mu_s = \frac{m_s + M_e}{M_e} \approx 1$ ,  $m_s$  [kg] is the mass of satellite, and  $M_e$  is the mass of Earth and  $\kappa_s \approx 1.9965 \cdot 10^7 [\frac{m^3}{s^2}]$ , is the gravitational constant of the Earth.

#### **Distance of the satellite from the center of the Earth.**

The true anomaly,  $f_{cs}$  and  $e_c$  are used to calculate the distance of the satellite from the Earth using the Equation.

$$r_{sa} = \frac{a(1 - e_c^2)}{1 + e_c \cos f_{cs}} \quad (82)$$

The satellite is closest (perifocus) to the Earth at  $f_{cs}=0$ , thus:

$$r_s = a(1 - e_c^2) \quad (83)$$

and furthest point (apofocus) from the Earth at  $f_{cs} = \pi$  is given by:

$$r_{sp} = a(1 + e_c^2) \quad (84)$$

### Satellite position at time t.

Given the current time t, the position of the satellite is computed iteratively. First, the apparent anomaly  $E_{ap}$  is computed using:

$$E_{ap}\left(\frac{\pi}{180}\right) - e_c \sin E_{ap} = \frac{\kappa_s \sqrt{\mu_s}}{a_s^{\frac{3}{2}}}(t - T_p) \quad (85)$$

where  $T_p$  is the time at which the satellite was at perifocus. The iteration will follow the following Equations:

$$\begin{aligned} \text{I: Start } E_{ap}^0 &= \left(\frac{180}{\pi}\right) \frac{\kappa_s \sqrt{\mu_s}}{a_s^{\frac{3}{2}}}(t - T_p); \quad \text{where } \kappa_s=0 \\ \text{II: Set } E_{ap}^{\kappa_s+1} &= \frac{e_c \sin E_{ap}^{\kappa_s} - e_c E_{ap}^{\kappa_s} \cos E_{ap}^{\kappa_s} + E_{ap}^0\left(\frac{\pi}{180}\right)}{\left(\frac{\pi}{180}\right) - e_c E_{ap}^{\kappa_s}} \\ \text{III: If } \frac{E_{ap}^{\kappa_s+1} - E_{ap}^{\kappa_s}}{|E_{ap}^{\kappa_s}|} &< 10^{-5} \quad \text{stop;} \end{aligned}$$

Otherwise, set  $\kappa_s = \kappa_s + 1$

and repeat stage II above.

(86)

The true anomaly is calculated from,

$$\cos f_{cs} = \frac{\cos E_{ap} - e_c}{1 - e_c \cos E_{ap}} \quad (87)$$

Or:

$$\sin f_{cs} = \frac{\sqrt{1 - e^2} \sin E_{ap}}{1 - e_c \cos E_{ap}} \quad (88)$$

### 7.2.2 Right Ascension-Declination coordinate system

Better calculations involving space points require an inertial or fixed coordinate system. The appropriate astrodynamical coordinate system is the  $\alpha - \delta$  coordinate system. In this system, the origin is fixed at the center of the Earth, the x-axis, (with unit vector  $\mathbf{i}$ ) points to the vernal equinox and the y-axis (with unit vector  $\mathbf{j}$ ) is perpendicular to the x-axis. Both are aligned on the equatorial plane. The z-axis (with unit vector  $\mathbf{k}$ ) points to the north as shown in Figure 37.

In this coordinate system, if  $[x, y, z]$  are given,  $[\alpha, \delta, r]$  can be computed using;

$$\begin{aligned} r &= \sqrt{x^2 + y^2 + z^2} \\ \cos \delta &= \frac{x^2 + y^2}{r} \quad \text{OR} \\ \sin \delta &= \frac{z}{r} \quad \text{and} \\ \cos \alpha &= \frac{x}{\sqrt{x^2 + y^2}} \quad \text{Or} \\ \sin \alpha &= \frac{y}{\sqrt{x^2 + y^2}} \end{aligned}$$

And the reverse transformation Equations are given as:

$$\begin{aligned} x &= r \cos \delta \cos \alpha \\ y &= r \cos \delta \sin \alpha \\ z &= r \sin \delta \end{aligned} \quad (89)$$

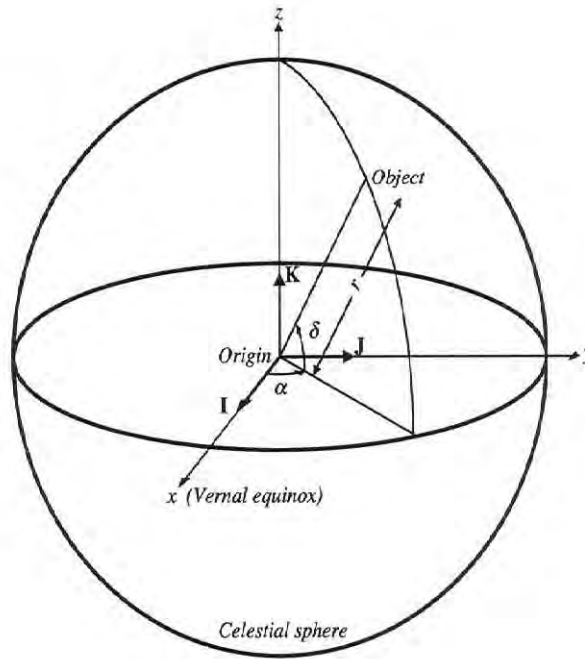


Figure 37: Right Ascension-Declination coordinate system

### 7.2.3 Satellite Orbit orientation in space

If the orbital-plane coordinate system is defined by the unit vectors,  $[\mathbf{P}, \mathbf{Q}, \mathbf{W}]$ , then, the orientation of the satellite in space with respect to an inertial frame of reference is specified with the  $\alpha - \delta$  system, see Figure 38. The following terms refer to the parameters needed for transformation.

**Orbital Inclination**, ( $0^\circ \leq i \leq 180^\circ$ ) - This is the angle between orbital and equatorial planes measured in a plane perpendicular to a line defining their respective intersection.

**Longitude of the ascending node, ( $0^0 \leq \Omega \leq 360^0$ )** - This is the angle measured in the orbital plane between the vernal equinox and the line defining the intersection of the orbital and equatorial planes as the point traverses through the equator from -z to +z.

**Argument of Perigee, ( $0^0 \leq \omega \leq 360^0$ )** - This is the angle measured in the orbital plane from the line defined by the longitude of the ascending node to another line in the orbital plane, containing the focus and passes through the perigee.

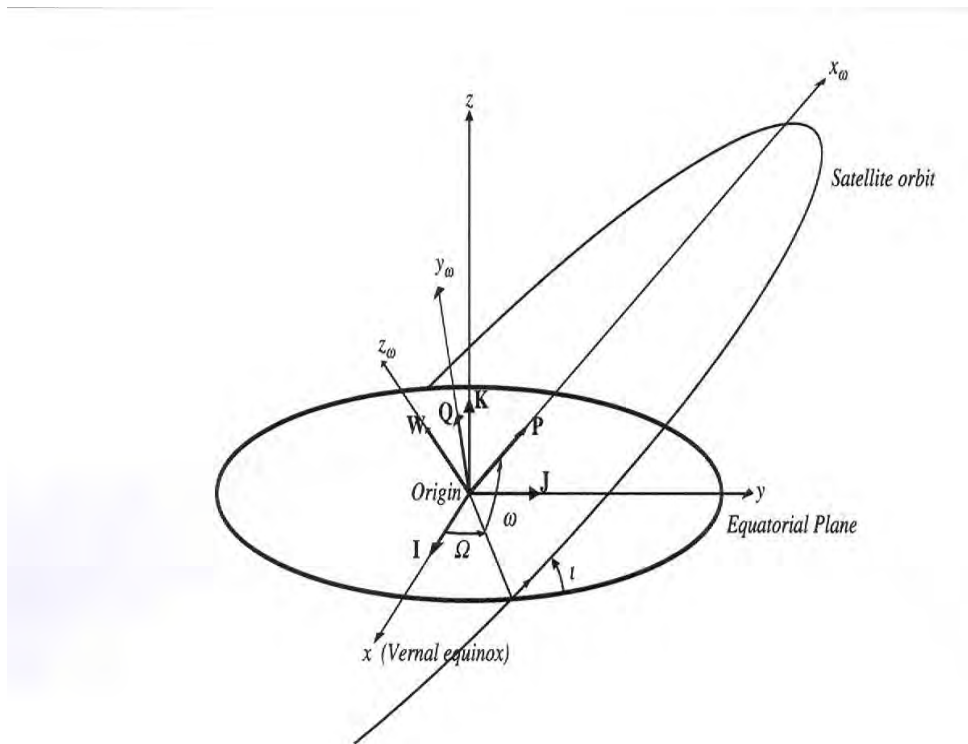


Figure 38: Orbit orientation in  $\alpha - \delta$  coordinate system

The following conversions can be carried out:

$$\begin{vmatrix} \mathbf{P} \\ \mathbf{Q} \\ \mathbf{W} \end{vmatrix} = \begin{vmatrix} \cos \omega & \sin \omega & 0 \\ -\sin \omega & \cos \omega & 0 \\ 0 & 0 & 1 \end{vmatrix} \begin{vmatrix} 1 & 0 & 0 \\ 0 & \cos i & \sin i \\ 0 & -\sin i & \cos i \end{vmatrix} \begin{vmatrix} \cos \Omega & \sin \Omega & 0 \\ -\sin \Omega & \cos \Omega & 0 \\ 0 & 0 & 1 \end{vmatrix} \begin{vmatrix} \mathbf{I} \\ \mathbf{J} \\ \mathbf{K} \end{vmatrix}$$

The inverse transformation is given as:

$$\begin{vmatrix} \mathbf{I} \\ \mathbf{J} \\ \mathbf{K} \end{vmatrix} = \begin{vmatrix} \cos \Omega & -\sin \Omega & 0 \\ \sin \Omega & \cos \Omega & 0 \\ 0 & 0 & 1 \end{vmatrix} \begin{vmatrix} 1 & 0 & 0 \\ 0 & \cos i & -\sin i \\ 0 & \sin i & \cos i \end{vmatrix} \begin{vmatrix} \cos \omega & -\sin \omega & 0 \\ -\sin \omega & \cos \omega & 0 \\ 0 & 0 & 1 \end{vmatrix} \begin{vmatrix} \mathbf{P} \\ \mathbf{Q} \\ \mathbf{W} \end{vmatrix}$$

Since the position of satellite in space is also referenced to Earth based stations, the Earth fixed coordinate system can be related to the  $\alpha - \delta$  coordinate system. Here, the transformation requires the local sidereal time ( $\theta_g$ , [in degrees]) of any point on the surface of the Earth, see Figure 39. The local sidereal time (specially defined here as  $\theta$ ) is given by the sum of observer's east longitude  $\lambda_E$  and the Greenwich mean sidereal time (GMST),  $\theta_g$ ;

$$\theta = \theta_g + \lambda_E$$

where,

$$\theta_g(\Delta T) = \theta_g(0^h) + \Omega_e \cdot \Delta T; \quad \text{and}$$

$$\theta_g(0^h) = 24110^s.54841 + 8640184^s.812866 \cdot T_u + LAA; \quad \text{where}$$

$$LAA = 0^s.093104 \cdot T_u^2 - 6.2 \times 10^{-6} \cdot T_u^3 \quad \text{and}$$

$$T_u = \frac{d_u}{36525}$$

Here,  $\theta_g(0^h)$  is the greenwich sidereal time at  $0^h$  (midnight) of the coordinated universal time ( $UCT$ ); the greenwich mean time ( $GMT$ ).  $\Delta T$  is the

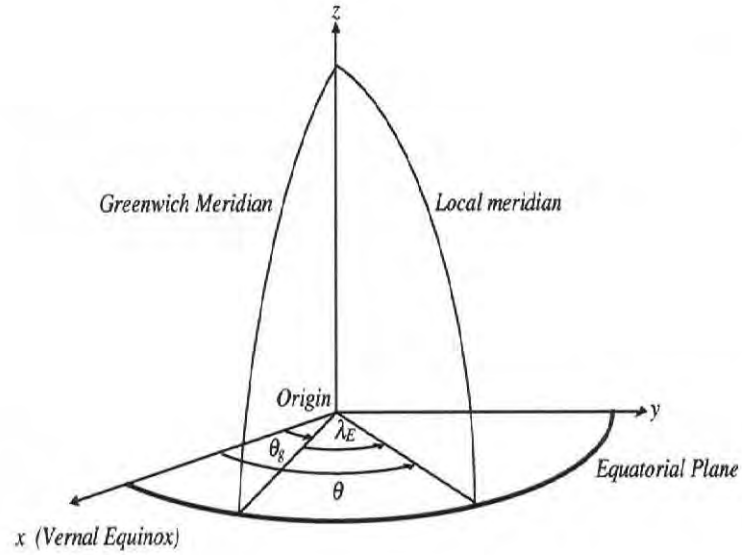


Figure 39: Sidereal and Local Sidereal time

UCT time of interest expressed in radians and  $\omega_e$  is the earth's rotation expressed in radians per second,  $d_u$  is the number of days of Universal Time (UT) elapsed since Julian Day (JD) 2451545.0, (2000-01-01, 12H00) [Kelso, 1995].

#### 7.2.4 Azimuth-Elevation coordinate system

This coordinate system places the satellite's orbital center on the surface of the Earth, (defined by a translation from the origin of the Earth) at

the observer position. This coordinate system co-rotates with the Earth's rotation since it is fixed with reference to the Earth. Three quantities are used to specify the position of the satellite, viz.

**Elevation**, ( $-90^0 \leq h \leq 90^0$ ) - The angular position of the satellite above the observer's horizon.

**Azimuth**, ( $0^0 \leq A \leq 360^0$ ) - The angle from the north to the satellite's meridian, measured in the observer's horizontal plane.

**Slant range**, ( $\rho_h$ ) - The distance between the observer and the satellite.

### 7.3 Satellite coordinate system transformation

Calculation of navigation parameters such as performance index of satellites, footprint, and antenna direction require that the observer and/or receiver be on different coordinate systems. Antenna direction and performance is best done if the satellite position is specified in Azimuth-Elevation coordinate system. If the satellite is represented in the LLA coordinate system, footprint radius is easily computed. This implies that transformations between different coordinate systems are necessary. I outline one kind of transformation only.

#### **Right Ascension-Declination to Azimuth-Elevation transformation**

Given the satellite coordinates  $(x,y,z)$  or  $(\alpha, \delta, r)$ , in the right ascension-declination system, and the ground station coordinates  $(\phi, \lambda_E, H, t)$ , the satellite azimuth-elevation coordinates,  $(A, h, \rho_h)$  can be computed as follows:

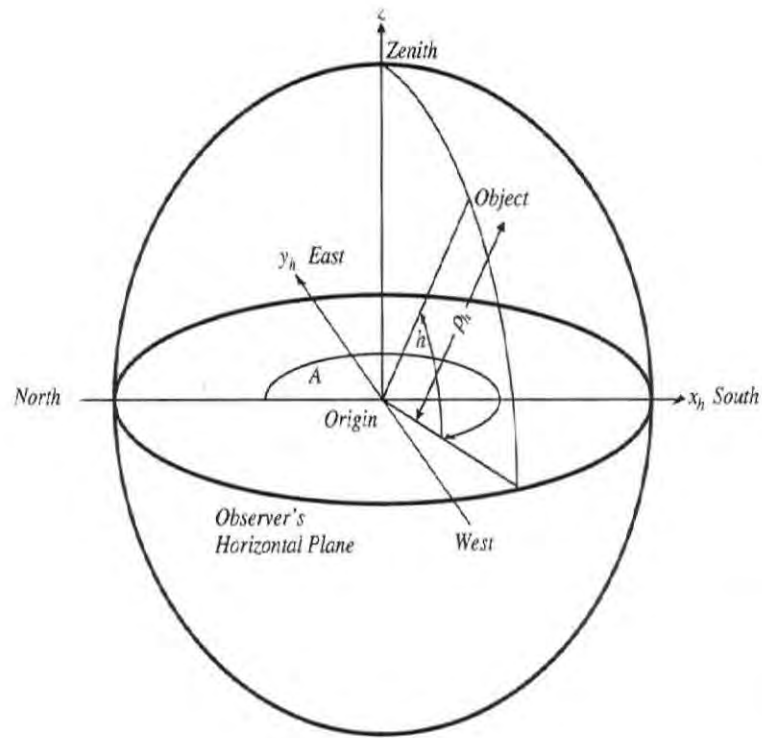


Figure 40: Azimuth-Elevation Coordinate system. The position of the satellite (designated as object) is specified with respect to position of the observer coordinates.)

**a** - Compute the station's sidereal time,  $\theta$ , from  $\lambda_E$  and time,  $t$ .

**b** - Compute:

$$G1 = \frac{a}{\sqrt{1 - (2f - f^2) \sin^2 \phi}} + H$$

$$G2 = \frac{a(1 - f^2)}{\sqrt{1 - (2f - f^2) \sin^2 \phi}} + H$$

$$x_0 = G1 \cos \phi \cos \theta$$

$$y_0 = G1 \cos \phi \cos \theta$$

$$z_0 = G2 \sin \phi$$

$$\rho_x = x - x_0$$

$$\rho_y = y - y_0$$

$$\rho_z = z - z_0$$

where,  $H$  is the station's elevation angle above sea-level, and  $f$  = the flattening factor of the Earth, see Table 10.

**c** -Distance between the satellite and the ground station is given by:

$$\rho_h = \sqrt{\rho_x^2 + \rho_y^2 + \rho_z^2}$$

And:

$$\begin{vmatrix} L_{xh} \\ L_{yh} \\ L_{zh} \end{vmatrix} = \begin{vmatrix} \sin \phi \cos \theta & \sin \theta \sin \theta & -\cos \phi \\ -\sin \theta & \cos \theta & 0 \\ \cos \theta \cos \phi & \sin \theta \cos \phi & \sin \phi \end{vmatrix} \begin{vmatrix} \frac{\rho_x}{\rho_h} \\ \frac{\rho_y}{\rho_h} \\ \frac{\rho_z}{\rho_h} \end{vmatrix}$$

**d** - The elevation is computed from:

$$\sin h = L_{zh}$$

$$\cos h = \sqrt{1 - L_h^2}$$

**e** -The azimuth is obtained from:

$$\sin A = \frac{L_{yh}}{\sqrt{1 - L_{zh}^2}}$$

$$\cos A = \frac{L_{xh}}{\sqrt{1 - L_{zh}^2}}$$

(90)

## References

1. [Adam, 2003]

Adam, R.M.: The South African Square Kilometer Array. Evaluation of Troposphere and Ionosphere for SKA sites. A supplementary report to ISSC. (2003).

2. [Aller, 2001]

Aller, H.D.: Interferometers and aperture synthesis: Radio astronomical instrumentation and techniques, (2001).

3. [Bilitza, 2003]

Bilitza, D.: International reference ionosphere 2000: Examples of improvements and new features. *Adv.Space Res.* Vol.31 , No.3, pp.757-767, (2003).

4. [Bilitza et al, 1998]

Bilitza, D, Koblinsky, C., Williamson, R., Bhardwaj, S.: Improving the topside electron density model for IRI. *Adv. Space Res.* Vol.22, No.6. pp.777-787, (1998).

5. [Brunner, 1991]

Brunner, F.K.: An improved model of the dual frequency ionospheric correction of GPS observations. *Manuscriptica geodetica*, vol. 16, pp. 205-214, (1991).

6. [Budden, 1985]  
Budden, K.G.: The Propagation of radio waves: The theory of radio waves of low power in the ionosphere and magnetosphere. Cambridge university press, (1985).
7. [Cilliers, 2005]  
Cilliers, P.J.: An Extended Chapman Profile. Private communication, (2005).
8. [Ciraolo and Spalla, 2002]  
Ciraolo, L. and Spalla, P.: TEC analysis of IRI simulated data, Adv. Space Res., Vol.29, No.6, pp.959-966, (2002).
9. [Dana, 1999]  
Dana, T.H.: Goedetic Datums. [www.colorado.edu/geography/gcraft/notes/datum/datum-ftoc.html](http://www.colorado.edu/geography/gcraft/notes/datum/datum-ftoc.html), (1999).
10. [Davies, 1990]  
Davies, K.: Ionospheric Radio. Peter Peregrinus ltd. (1990)
11. [Feltens, 1998]  
Feltens, J.: Chapman Profile Approach for 3-D Global TEC representation. ESA, European Space operations Centre, Germany, (1998).
12. [Fomalont, 1995]  
Fomalont, E.: Astronomy. Very Long Baseline Interferometry and the VLBA ASP Conference Series, vol. 82, (1995).

13. [Gao and Liu., 2002]  
Gao, L., Liu, L.L.: Precise Ionosphere Modelling Using Regional GPS Network Data. *J. Global Positioning Systems.*, vol.1, no.1, pp.18-24, (2002)
14. [Goodwin et al, 1995]  
Goodwin, G. L., Silby, J. H., Lynn, K. J. W., Breed, A. M., Essex, E. A.: GPS satellite measurements: Ionospheric slab thickness and total electron content, *J. Atmos. Terr. Phys.*, vol.57, No.14, pp.1723-173,(1995).
15. [Haniff, 2002]  
Haniff, C.A.: Introduction to Interferometry. EuroWinter school, Feb 3-8, (2002).
16. [Hunsucker and Hargreaves., 2003]  
Hunsucker, R.D., Hargreaves, J.K.: *The High-Latitude Ionosphere and its Effects on Radio Propagation.* University Press, Cambridge. pp.2, (2003).
17. [Hofmann-Wellenhof et al, 1997]  
Hofmann-Wellenhof, B.H., Lichtenegger, H., Collins, J.: *GPS Theory and Practice* (4th ed). Springer, Berlin, (1997).
18. [Kaplan, 1998]  
Kaplan, H.G.: High precision algorithms for Astrometry: A comparison of two approaches. *The Astr. Journal*, vol. 115, pp. 361-372, (1998).

19. [Kelso, 1995]  
Kelso, T.S., Orbital Coordinate systems. <http://celestrak.com>, (1995).
20. [Kondo, 1991]  
Kondo, T.: Application of VLBI data to measurement of ionosphere TEC. Journal of Comm. Res. Lab, vol. 38, pp. 613-622, (1991).
21. [Klobuchar, 2001]  
Klobuchar, J. A.: Ionospheric effects on GPS. Geoph. directorate, ionospheric effects division, Philips Lab. Massachusetts, (2001).
22. [Mamoru et al, 2003]  
Mamoru, S., Kondo, T., Kawai, E.: Evaluation of GPS based ionospheric TEC map by comparing with VLBI data. Radio Sci., 38(4), 1069, doi: 10.1029/2000RS002620, (2003).
23. [Milan, 2004]  
Milan, S.: The Thermosphere and Ionosphere. PPARC Introductory course on Solar Terrestrial Physics, University of Leicester, (2004).
24. [Middelberg et al, 2005]  
Middelberg, E.M., Roy, A.L., Walker, R.C., Falcke, H.: VLBI observations of weak radio sources using fast frequency switching. Astron. and Astrophys.,. A preprint doi:10.1051/004-6361:20042078. ESO ©, (2005).

25. [Opperman and Cilliers., 2004]  
Opperman, B.D.L., Cilliers, P.J.: Ionospheric characterisation using dual frequency GPS receivers: Short Course, Rhodes University, (2004).
26. [Perley and Bust, 2002]  
Perley, R., Bust, G.: Probing the ionosphere with the very large array. URSI General Assembly, Maastrich, The Netherlands, (2002).
27. [Pérez-Torres et al, 2000]  
Pérez-Torres, M.A., Marcaide, J.M., Guirado, J.C., Ros, E., Shapiro, I.I., Ratner, M.I. and Sardón, E.: Towards global phase-delay VLBI astrometry: observations of QSO 1150+812 and BL 1803+784. *J. Astron. Astrophys.*, 360, pp.161-170, (2000).
28. [Richmond, 1995]  
Richmond, A.: The ionospheric wind dynamo: effects of its coupling with different atmospheric regions, *The Upper Mesosphere and Lower Thermosphere: A review of Experiment and Theory*, Geophys. Monograph. vol. 87, pg. 49-65, edited by Johnson, R. and Killeen, T.: AGU, Washington D.C. (1995).
29. [Stanimir et al, 2003]  
Stanimir, M., Stankov, M., Norbert, J., Haise, S., Muhtarov, P., Kutiiev, I., Warnant, R.: A new method for reconstruction of the vertical electron content density distribution in the upper ionosphere and plasmasphere, *J.Geophys Res.*, 108(A5), pp.1164, (2003).

30. [Taylor, 1999]  
Taylor, A.T.: The Square Kilometer Array: A science overview. University of Calgary, (Alberta). Edited by: Haarlem, V.P.M.: Netherlands Foundation for Research in Astronomy, (1999).
31. [Vincenty, 1980]  
Vincenty, T.: On the transformation from Three-Dimensional to Ellipsoidal Coordinates. Zeitschrift fuer Vermessungswesen, Stuttgart, Germany. (1980).
32. [Yuzef-Zadeh et al, 1999]  
Yuzef-Zadeh, F., Choate, D., Cotton, W.: The position of Sagittarius A\* at the galactic center. Astro. Journal, (1999).
33. [Wanninger, 1994]  
Wanninger, L.: Der Einfluss der Ionosphäre auf die Positionierung mit GPS. ISSN 0174-1454, Universität Hannover, (1994).
34. [Withels, 1975]  
Withels, J. J.: A two-element interferometer. A PhD thesis, Massachusetts Institute of Technology, (1975).